



Decoding the spatial spread of cyanobacterial blooms in an epilimnion

Jacob Serpico¹ · Kyung-Han Choi¹ · B. A. Zambrano-Luna¹ · Tian Xu Wang¹ · Hao Wang¹

Received: 17 February 2025 / Revised: 12 July 2025 / Accepted: 27 July 2025

© The Author(s), under exclusive licence to Springer-Verlag GmbH Germany, part of Springer Nature 2025

Abstract

Cyanobacterial blooms (CBs) pose significant global challenges due to their harmful toxins and socio-economic impacts, with nutrient availability playing a key role in their growth, as described by ecological stoichiometry (ES). However, real-world ecosystems exhibit spatial heterogeneity, limiting the applicability of simpler, spatially uniform models. To address this, we develop a spatially explicit partial differential equation model based on ES to study cyanobacteria in the epilimnion of freshwater systems. We establish the well-posedness of the model and perform a stability analysis, showing that it admits two linearly stable steady states, leading to either extinction or a spatially uniform positive equilibrium where cyanobacterial biomass stabilizes at its carrying capacity. Further, we discuss the possibility of long-term spatially nonuniform solution with small diffusion and space-dependent parameters. We use the finite elements method (FEM) to numerically solve our system on a real lake domain derived from Geographic Information System (GIS) data and realistic wind conditions extrapolated from ERA5-Land. Additionally, we use a cyanobacteria estimation (CE) obtained from Sentinel-2 to set initial conditions, and we achieve strong model validation metrics. Our numerical results highlight the importance of lake shape and size in bloom monitoring, while global sensitivity analysis using Sobol Indices identifies light attenuation and intensity as primary drivers of bloom variation, with water movement influencing early bloom stages and nutrient input becoming critical over time. This model supports continuous water-quality monitoring, informing agricultural, recreational, economic, and public health strategies for mitigating CBs.

Keywords Cyanobacteria · Partial differential equations · Ecological stoichiometry · Stability analysis · Finite elements method

Extended author information available on the last page of the article

1 Introduction

Cyanobacteria are photosynthetic prokaryotes that increasingly dominate nutrient-rich freshwater systems. Many bloom-forming taxa synthesize potent toxins, such as microcystin, compromising drinking-water safety, harming wildlife, and curtailing recreation (Paerl and Huisman 2008; Huisman et al. 2018). Rising temperatures, altered hydrology, and continued nutrient enrichment have amplified the frequency and magnitude of these blooms globally (Paerl and Huisman 2009; Wilhelm et al. 2011).

Existing modelling efforts show that ecological stoichiometry provides a robust framework for understanding nutrient-driven population growth and species interactions (Heggerud et al. 2020). For cyanobacteria, stoichiometric constraints often center on intracellular phosphorus content and its interaction with light, temperature, and other ecological parameters. Although several ordinary differential equation (ODE) models have shed light on stoichiometric constraints in plankton species (Wang et al. 2007), many freshwater ecosystems exhibit pronounced spatial heterogeneity due to gradients in nutrient concentrations, light availability, and water movement. As a result, partial differential equations (PDEs) can more accurately capture the spatiotemporal patterns arising from organism movement and resource flow (Cantrell and Cosner 2004). Specifically, incorporating diffusion, advection, and vertical or horizontal mixing processes can offer deeper mechanistic insights into how blooms initiate and spread and how nutrient supply interacts with spatially varying environmental conditions (Huisman and Weissing 1994; Cao et al. 2006).

We propose and analyze a reaction-diffusion-advection model that incorporates ecological stoichiometry to study the interactions among cyanobacterial biomass, intracellular phosphorus, and dissolved mineral phosphorus. While previous studies such as Hsu et al. (2010, 2014, 2017) have focused on nutrient stoichiometry in a vertical unstirred chemostat domain, our interest lies in understanding horizontal heterogeneity in large lakes. We chose to study Pigeon Lake, Alberta, Canada which has a somewhat oval shape with few embayments; there are no extreme sub-basins or islands, and horizontal depth differences are moderate. This morphometry is relatively simple. Aside from a slight gradient of deeper water toward the centre, we did not have pronounced depth-driven habitat heterogeneity to analyze. By modelling these dynamics, we aim to better understand the movement of cyanobacteria, which can be observed through satellite imagery. To achieve this, we introduce a system of equations that account for horizontal diffusion and advection in the lake's epilimnion, assuming a constant diffusion rate in the horizontal domain.

Our work focuses on three major components. First, we formulate and rigorously analyze a mechanistic model and establish the well-posedness of the system in a bounded domain by proving the global existence, uniqueness, and boundedness of solutions under biologically relevant assumptions. Second, we investigate the long-term behaviour of the model through rigorous stability analysis of equilibrium states, identifying conditions under which cyanobacteria persist or die out. We conduct extensive numerical simulations to investigate the spatial dynamics in one- and two-dimensional spatial domains. We employ finite-difference schemes in one- and two-dimensions to illustrate key wavefront, boundary-layer, and long-term

spatial heterogeneity. Additionally, for the two-dimensional case, we utilize the finite element method on a lake-shaped domain to improve realism, where spatial heterogeneity and irregular boundary geometry can strongly influence bloom formation and nutrient distribution. Both one- and two-dimensional simulations incorporate a function interpolated to real wind data. Specifically, we extract hourly wind vectors for the grid cell centred on Pigeon Lake, Alberta, Canada, 2023 from the ERA5-Land reanalysis ($0.1^\circ \times 0.1^\circ$ resolution ≈ 11 km) (Munoz Sabater 2019). Then, we average the directional components to daily means. We map the smoothed series onto the simulation window and convert it to a continuous function of model time via cubic-spline interpolation. The resulting fields are spatially uniform across the lake domain. To set the initial cyanobacterial biomass field and validate the finite elements method (FEM) simulation, we used the dataset generated by Zambrano-Luna et al. (2025) using a combination of machine learning and multispectral images from Sentinel-2. For the initial condition, we selected the scene dated August 6, 2023.

Given that parameter uncertainty is often significant in real freshwater systems, we conduct a global sensitivity analysis to identify which physical parameters, such as epilimnion depth, water exchange rate, and background light attenuation, have the most significant influence on cyanobacteria dynamics. Our results reveal how spatially heterogeneous resource distributions, wind-driven advection, physical lake conditions, and nutrient dynamics shape the persistence or collapse of a cyanobacteria population. We discuss how these findings have implications for water resource management, providing guidance on which parameter regimes may be most critical to monitor or control in the context of bloom prevention and mitigation efforts.

2 Model formulation

Numerous models exist that investigate the qualitative dynamics of generic bloom-forming cyanobacteria such as *Microcystis aeruginosa* in a spatially homogeneous environment. One such model by Heggerud et al. (2020) proposed the following stoichiometric equation for the growth of cyanobacteria,

$$\frac{dB}{dt} = rB \left(1 - \frac{Q_m}{Q} \right) h(B) - lB - \frac{D}{z_m} B, \quad (1)$$

where B and Q describe the concentration of carbon biomass of cyanobacteria and intracellular (internal) phosphorus-to-carbon cell quota (p/B), respectively. Both nutrients and light limit the logistic growth of cyanobacteria. The empirically validated Droop form models the former and the latter by the ubiquitous Monod form. The difference in mathematical expression stems from the two forms of energy being absorbed and processed differently (Wang et al. 2022). Adhering to the Lambert-Beer law (Huisman and Weissing 1994), with r representing the growth rate, the light intensity at the depth s of a water column with cyanobacterial abundance B is

$$I(s, B) = I_{\text{in}} \exp[-(K_{\text{bg}} + kB)s]. \quad (2)$$

We assume the epilimnion is well mixed overnight (Heggerud et al. 2020; Wang et al. 2007). Thus, the depth-averaged cyanobacterial growth function contains the factor

$$h(B) = \frac{1}{z_m} \int_0^{z_m} \frac{I(s, B)}{I(s, B) + H} ds = \frac{1}{z_m(kB + K_{bg})} \ln \left(\frac{H + I_{in}}{H + I(z_m, B)} \right). \quad (3)$$

The parameters I_{in} , K_{bg} , and k are described in Table 1. Cyanobacteria uptake nutrients from the environment and lose nutrients through dilution due to growth. The nutrient uptake function is given by

$$\rho(Q, P) = \rho_m \left(\frac{Q_M - Q}{Q_M - Q_m} \right) \frac{P}{P + M}, \quad (4)$$

where ρ_m , M , and P are the maximum phosphorus uptake rate, the half-saturation coefficient for cyanobacteria phosphorus uptake, and the concentration of mineral phosphorus in the epilimnion (external phosphorus), respectively. The parameter l represents the loss rate of cyanobacteria due to respiration and other factors. The other parameters are given in Table 1.

Table 1 Parameters and their respective meanings and units used in the model.

Parameter	Meaning	Value	References
α	Cyanobacterial diffusion coefficient	0.0001–0.1 m ² /day	Estimated
β	Dissolved phosphorus diffusion coefficient	0.0002–0.2 m ² /day	Estimated
β_B	Cyanobacterial advection scalar	0.01–1	Estimated
β_P	Dissolved phosphorus advection scalar	0.02–2	Estimated
r	Maximum cyanobacterial production rate	0.7–1.1/day	Diehl et al. (2005)
Q_m	Cyanobacterial cell quota at which growth ceases	0.004 mgP/mgC	Diehl et al. (2005)
Q_M	Cyanobacterial cell quota at which nutrient uptake ceases	0.004 mgP/mgC	Diehl et al. (2005)
z_m	Depth of epilimnion	> 0–10 m	Kalff (2002)
k	Cyanobacterial-specific light attenuation	0.0003–0.0004 m ² /mgC	Diehl et al. (2005)
K_{bg}	Background light attenuation	0.3–0.9/m	Diehl et al. (2005)
H	Half-saturation coefficient of light-dependent production	120 μ mol/(m ² day)	Diehl et al. (2005)
I_{in}	Light intensity at the surface of the water	300 μ mol/(m ² day)	Diehl et al. (2005)
l	Loss of cyanobacterial due to respiration	0.05–0.6/day	Berger et al. (2006)
D	Water exchange between stratified lake layers	0.02 m/day	Berger et al. (2006)
ρ_m	Maximum cyanobacterial phosphorus uptake rate	1 mgP/mgC/day	Diehl et al. (2005)
P_h	Dissolved mineral phosphorus concentration in hypolimnion	0–150 mgP/m ²	Berger et al. (2006)
M	Half-saturation coefficient for cyanobacterial nutrient uptake	1.5 mgP/m ²	Diehl et al. (2005)

Existing modelling efforts incorporating ecological stoichiometry are commonly explored using ODE frameworks. However, empirical evidence suggests that environments' spatial scale and structure can significantly influence population interactions (Cantrell and Cosner 2004). Thus, extending the existing ODE model to apply to a spatially heterogeneous environment is a natural step. In this study, we formulate a mechanistic reaction-diffusion-advection PDE model to investigate the dynamics of cyanobacteria in a spatially heterogeneous lake. To provide an accurate and versatile model that can be fitted to various data exports, we take a top-down view of a lake and consider it within the bounded domain $\Omega \subset \mathbb{R}^2$. We consider a lake with two layers: the epilimnion and the hypolimnion. The epilimnion, with an assumed depth of z_m , is where cyanobacteria predominantly reside. Below the epilimnion lies the hypolimnion, a deeper layer typically more stable and less affected by surface conditions. The stratification between these two layers affects the transport and mixing of nutrients, as well as the movement of cyanobacteria. Since cyanobacteria generally do not sink unless they are deceased (Zhao and Huang 2014; Cao et al. 2006), we assume their population exists idly (without external force) in the epilimnion layer.

Notably, since Q is not a physical quantity but a ratio, it is more reasonable to track intracellular (p) and dissolved mineral (P) phosphorus as spatially heterogeneous quantities within the model. Three principal mechanisms drive cyanobacterial and phosphorus transport. First, cyanobacteria are unicellular and lack flagella or any other means of active horizontal transport, so they move as passive tracers of ambient water turbulence (Okubo and Levin 2002; Deng et al. 2016). Consequently, our model assigns horizontal diffusion coefficients, α for cyanobacteria and β for phosphorus. Constant coefficients also help retain analytical tractability while capturing the dominant mixing process. Within the epilimnion layer, cyanobacterial directional movement is determined by water affected by wind (Cao et al. 2006; Zhang et al. 2021), with a vector $\vec{v} = (u(t), v(t)) \in \mathbb{R}^2$ describing the wind movement. We consider water exchange between the epilimnion and hypolimnion, with a water exchange rate of D . The nutrients and cyanobacteria will sink or become buoyant due to the force of this water exchange. Following Heggerud et al. (2020), the water exchange rate is inversely proportional to the depth of the epilimnion. On the other hand, since the hypolimnion in a lake is significant and stable enough, the phosphorus variation in the hypolimnion can be considered negligible, and we assume the phosphorus concentration is constant at P_h . Hence, $\frac{D}{z_m} (P_h - P)$ indicates the vertical exchange through the thermocline from the hypolimnion to the epilimnion. If $P_h > P$, there is an extra phosphorus input from the hypolimnion to the epilimnion; otherwise, the phosphorus concentration will be diluted.

Based on the above discussion, the full model on $\Omega \times (0, \infty)$ is then given by

$$\left\{ \begin{array}{l} \frac{\partial B(x,t)}{\partial t} = \underbrace{\alpha \Delta B}_{\text{diffusion}} - \underbrace{\beta_B \vec{v}(t) \nabla B}_{\text{advection}} + \underbrace{r \left(1 - Q_m \frac{B}{p}\right) h(B) B}_{\text{limited growth term}} - \underbrace{lB}_{\text{loss}} - \underbrace{\frac{D}{z_m} B}_{\text{vertical exchange}}, \\ \frac{\partial p(x,t)}{\partial t} = \underbrace{\alpha \Delta p}_{\text{diffusion}} - \underbrace{\beta_B \vec{v}(t) \nabla p}_{\text{advection}} + \underbrace{\eta(B, p, P)}_{\text{uptake by bacteria}} - \underbrace{lp}_{\text{phosphorus loss}} - \underbrace{\frac{D}{z_m} p}_{\text{vertical exchange}}, \\ \frac{\partial P(x,t)}{\partial t} = \underbrace{\beta_P \Delta P}_{\text{diffusion}} - \underbrace{\beta_P \vec{v}(t) \nabla P}_{\text{advection}} + \underbrace{\frac{D}{z_m} (P_h - P)}_{\text{vertical exchange}} - \underbrace{\eta(B, p, P)}_{\text{uptake by bacteria}} + \underbrace{lp}_{\text{phosphorus recycling}}, \end{array} \right. \quad (\mathcal{S}_p),$$

with boundary and initial conditions

$$\begin{aligned} \partial_\nu B(x, t) = \partial_\nu p(x, t) = \partial_\nu P(x, t) = 0, \quad (x, t) \in \partial\Omega \times (0, \infty), \\ (B(x, 0), p(x, 0), P(x, 0)) = (B_0(x), p_0(x), P_0(x)), \quad x \in \Omega. \end{aligned} \quad (5)$$

Here, B (mgC/m²) represents the concentration of cyanobacterial biomass, and

$$\eta(B, p, P) = \rho_m \left(\frac{Q_M B - p}{Q_M - Q_m} \right) \frac{P}{P + M}.$$

Using this function, we remove the singularity of the original function $\rho(p/B, P)$. The remaining parameters are provided in Table 1.

3 Dynamical analysis

3.1 Assumptions

(A_I) The initial conditions B_0, p_0, P_0 satisfy

$$(B_0, p_0, P_0) \in [W^{2,\infty}(\Omega)]^3, B_0, p_0, P_0 > 0, \text{ and } Q_m \leq \frac{p_0}{B_0} \leq Q_M.$$

(A_C) All parameters in the model are positive constants.

3.2 Well-posedness

For biological rationality, it is necessary to show the well-posedness of the solutions to the model. Therefore, we devote this section to studying the existence and uniqueness of model (\mathcal{S}_p). We introduce the following lemma to resolve the challenge from the unboundedness of the reaction term in the first equation.

Lemma 3.1 *Assume that (A_I), (A_C), and $(B, p, P) \in C^{2,1}(\bar{\Omega} \times (0, T_{\max}); \mathbb{R}_+^3) \cap C^1(\bar{\Omega} \times (0, T_{\max}); \mathbb{R}_+^3)$ is a solution of the system (\mathcal{S}_p) – (5). Then it satisfies*

$$Q_m \leq \frac{p}{B} \leq Q_M \text{ in } \bar{\Omega} \times [0, T], \quad T < T_{\max}. \quad (6)$$

Proof We first prove the $Q_m \leq \frac{p}{B}$. Let $y = p - Q_m B$ and $y(\cdot, 0) = p_0 - Q_m B_0 \geq 0$ by (A_I) . Then it follows that

$$\partial_t y - \alpha \Delta y + \beta_B \vec{v}(t) \nabla y + l y + \frac{D}{z_m} y - \rho(p/B, P) B + \frac{Q_m r}{p} h(B) B y = 0.$$

Define an operator $\mathcal{L}_1: C^{2,1}(\bar{\Omega} \times (0, T_{\max}); \mathbb{R}_+^3) \cap C(\bar{\Omega} \times [0, T_{\max}); \mathbb{R}_+^3) \rightarrow C(\bar{\Omega} \times [0, T_{\max}); \mathbb{R}_+^3)$,

$$\begin{aligned} \mathcal{L}_1(y) &:= \partial_t y - \alpha \Delta y + \beta_B \vec{v}(t) \nabla y + l y + \frac{D}{z_m} y - \rho(p/B, P) B + \frac{Q_m r}{p} h(B) B y \\ &= \partial_t y - \alpha \Delta y + \beta_B \vec{v}(t) \nabla y + l y + \frac{D}{z_m} y + \frac{\rho_m}{Q_M - Q_m} \frac{P}{P + M} (y - (Q_M - Q_m) B) \\ &\quad + \frac{Q_m r}{p} h(B) B y. \end{aligned}$$

It's easy to check that,

$$\mathcal{L}_1(0) = -\rho_m \frac{P}{P + M} B \leq 0,$$

for each $(x, t) \in \bar{\Omega} \times [0, T_{\max})$. The standard comparison principle yields $y \geq 0$ in $\bar{\Omega} \times [0, T_{\max})$. Likewise, we can use a similar argument to prove the second inequality of (6). \square

Remark 3.1 Lemma 3.1 also holds for either B and p approaching 0.

Biologically, Q_m denotes the minimum phosphorus quota required for basic cellular maintenance, whereas Q_M represents the maximal intracellular storage capacity; keeping the ratio $p/B = Q$ within $[Q_m, Q_M]$ ensures that cyanobacteria remain physiologically viable and do not accumulate unrealistically large phosphorus reserves.

Lemma 3.2 (Local existence) *The system (\mathcal{S}_p) – (5) has a unique maximal solution $U = (B, p, P)$ satisfying*

$$U \in C^{2,1}(\bar{\Omega} \times (0, T_{\max}); \mathbb{R}_{\geq 0}^3) \cap C(\bar{\Omega} \times [0, T_{\max}); \mathbb{R}_+^3), \quad (7)$$

where $T_{\max} \in (0, \infty]$. If $T_{\max} < \infty$, then

$$\lim_{t \rightarrow T_{\max}} (||B(\cdot, t)||_{L^\infty} + ||p(\cdot, t)||_{L^\infty} + ||P(\cdot, t)||_{L^\infty}) = \infty. \quad (8)$$

Proof We consider auxiliary system given by

$$\partial_t U = \nabla(\mathbb{A} \nabla U) + \Phi(U, \nabla U), \quad (x, t) \in \Omega \times (0, \infty),$$

where $U = (B, p, P)$, $\mathbb{A} = \text{diag}\{\alpha, \alpha, \beta\}$ and

$$\Phi(U, \nabla U) = \begin{pmatrix} -\beta_B \vec{v}(t) \nabla B + r \left(1 - Q_m \frac{B}{p}\right) h(B) B - lB - \frac{D}{z_m} B \\ -\beta_B \vec{v}(t) \nabla p + \eta(B, p, P) B - lp - \frac{D}{z_m} p \\ -\beta_P \vec{v}(t) \nabla P + \frac{D}{z_m} (P_h - P) - \eta(B, p, P) B + lp \end{pmatrix}. \quad (9)$$

Fix $p > n$, $\epsilon > 0$ and define

$$V = \{v \in W^{1,p}(\Omega; \mathbb{R}^3) : v(x) \in G = (0, \infty)^3, \forall x \in \bar{\Omega}\}.$$

Since $\mathbb{A} = \text{diag}\{\alpha, \alpha, \beta\}$ and α, β are real positive numbers, then all its eigenvalues have positive real parts. Moreover, assumption (A_I) implies that the initial values belong to V . Therefore, the local existence of the solution U is guaranteed by (Amann and Crandall (1990), p. 17), where U satisfies

$$U \in C([0, T_{\max}), V) \cap C^{2,1}(\bar{\Omega} \times (0, T_{\max}), \mathbb{R}^3)$$

and $T_{\max} \in (0, \infty]$ is the lifespan defined by

$$T_{\max} := \sup\{T > 0 : U(\cdot, t) \in V, \forall t \in [0, T]\}.$$

By the Sobolev Embedding and the fact that $U(\cdot, t) \in C(\bar{\Omega}; \mathbb{R}^3)$ for all $t \geq 0$, we obtain

$$U \in C([0, T_{\max}), C(\bar{\Omega}; \mathbb{R}^3)) = C(\bar{\Omega} \times [0, T_{\max}); \mathbb{R}^3).$$

Since (S_p) is uniformly positive definite, together with assumption (A_I) , the solution to equation $(S_p) - (5)$ satisfies (Lemma 3.1 Wang et al. (2025))

$$B(x, t), p(x, t), P(x, t) > 0, \quad \forall (x, t) \in \bar{\Omega} \times (0, T_{\max}).$$

Then, (7) holds. In order to exclude the possibility that U approaches to ∂V as $t \rightarrow T_{\max}$ if $T_{\max} < \infty$, we prove U stays away from ∂V . Assume $T_{\max} < \infty$. Consider the auxiliary problem

$$\begin{cases} \partial_t \tilde{B} = \alpha \Delta \tilde{B} - \beta_B \vec{v}(t) \nabla \tilde{B} - l\tilde{B} - \frac{D}{z_m} \tilde{B} & \text{in } \Omega \times (0, \tilde{T}_{\max}) \\ \partial_\nu \tilde{B} = 0 & \text{in } \partial\Omega \times (0, \tilde{T}_{\max}) \\ \tilde{B}(x, 0) = B_0(x) & \text{on } \bar{\Omega}. \end{cases} \quad (10)$$

By Amann and Crandall (1990) and $B_0 > 0$ in $\bar{\Omega}$, there exists a unique nontrivial solution $\tilde{B} \in C^{2,1}(\bar{\Omega} \times (0, T_{\max})) \cap C(\bar{\Omega} \times [0, T_{\max}))$ of (10). One can easily show

that $0 \leq \tilde{B} \leq \|B_0\|_{L^\infty(\Omega)}$ in $\bar{\Omega} \times [0, \infty)$, which gives $\tilde{T}_{\max} = \infty$. Let $y = \tilde{B} - B$. Then y satisfies

$$\begin{cases} \partial_t y = \alpha \Delta y - \beta_B \vec{v}(t) \nabla y - l y - \frac{D}{z_m} y - r \left(1 - Q_m \frac{B}{p}\right) h(B) B & \text{in } \Omega \times (0, T_{\max}) \\ \partial_\nu y = 0 & \text{in } \partial\Omega \times (0, T_{\max}) \\ y(x, 0) = 0 & \text{on } \bar{\Omega}. \end{cases}$$

Due to Lemma 3.1, we have $\partial_t y - \alpha \Delta y + \beta_B \vec{v}(t) \nabla y + (l + \frac{D}{z_m}) y \leq 0$ in $\Omega \times (0, T_{\max})$. The maximum principle shows that $y \leq 0$ in $\bar{\Omega} \times [0, T_{\max})$, hence $\tilde{B} \leq B$ in $\bar{\Omega} \times [0, T_{\max})$. Harnack's inequality for parabolic equations (see Evans (2010)) ensures that for each $0 < t_1 < t_2$ and $K \subset\subset \Omega$, there exists a positive constant C such that

$$\sup_{x \in K} \tilde{B}(x, t_1) \leq C \inf_{x \in K} \tilde{B}(x, t_2).$$

For each $x \in \Omega$, we can choose K and $t < T_{\max}$ such that $\sup_{x \in K} \tilde{B}(x, t) > 0$. Then we have $0 < \sup_{x \in K} \tilde{B}(x, t) < C \inf_{x \in K} \tilde{B}(x, T_{\max})$, which implies $\tilde{B}(x, T_{\max}) > 0$. If $x \in \partial\Omega$ and $\tilde{B}(x, t) = 0$, Hopf's lemma yields a contradiction to the fact that $\partial_\nu \tilde{B} = 0$ on $\partial\Omega$. Therefore, $\tilde{B}(x, t) > 0$ over $\bar{\Omega} \times [0, T_{\max}]$. In conclusion, for each $x \in \bar{\Omega}$

$$\liminf_{t \rightarrow T_{\max}} B(x, t) \geq \tilde{B}(x, T_{\max}) > 0.$$

By using similar arguments, we can show p and P do not approach zero as $t \rightarrow T_{\max}$, so that the solution $U = (B, p, P)$ stays away from ∂V , which concludes that (8) holds by Amann and Crandall (1990). \square

3.3 L^∞ boundedness

Lemma 3.3 Assume that (A_I) and (A_C) . Then there exists a constant \bar{B} such that the solution to equation $(S_p) - (5)$ satisfies

$$B(x, t) \leq \max\{\|B_0\|_{L^\infty(\bar{\Omega})}, \bar{B}\}, \quad \text{for all } (x, t) \in \bar{\Omega} \times [0, T_{\max}]. \quad (11)$$

Proof From equation (3), (2), and Lemma 3.1, we obtain

$$h(B) \leq \frac{1}{z_m(kB + K_{bg})} \left(\frac{Q_M - Q_m}{Q_M} \right) \ln \left(\frac{H + I_{\text{in}}}{H} \right).$$

It follows from the positivity of B and p , the first equation of (S_p) imply that

$$\partial_t B - \alpha \Delta B + \beta_B \vec{v}(t) \nabla B \leq f(B) \quad \text{in } \Omega \times (0, T_{\max}), \quad (12)$$

where

$$f(B) = \left(\frac{r}{z_m(kB + K_{bg})} \left(\frac{Q_M - Q_m}{Q_M} \right) \ln \left(\frac{H + I_{in}}{H} \right) - l - \frac{D}{z_m} \right) B.$$

Let us denote by a nonzero constant \bar{B} such that $f(\bar{B}) = 0$. Then either $\bar{B} < 0$ or $\bar{B} > 0$ for different parameters of f . If $\bar{B} < 0$, $f(B) < 0$ for all $(x, t) \in \Omega \times (0, T_{\max})$. Then the maximum principle and (A_I) show that $B \leq \|B_0\|_{L^\infty}$. (only if $\partial\Omega \in C^{2,1}$.) If $\bar{B} > 0$, notice that $f(B) \leq 0$ for all $B \geq \bar{B}$. Let us define an operator $\mathcal{L}_2 : C^{2,1}(\bar{\Omega} \times (0, T_{\max})) \cap C(\bar{\Omega} \times [0, T_{\max})) \rightarrow C(\bar{\Omega} \times [0, T_{\max}))$, with

$$\begin{aligned} \mathcal{L}_2(B) &= \partial_t B - \alpha \Delta B + \beta_B \vec{v}(t) \nabla B - r \left(1 - \frac{Q_m B}{p} \right) h(B) B - l B - \frac{D}{z_m} B \\ &\geq \partial_t B - \alpha \Delta B + \beta_B \vec{v}(t) \nabla B - f(B). \end{aligned}$$

Then $\mathcal{L}_2(C) \geq 0$ for $C = \max\{\|B_0\|_{L^\infty(\bar{\Omega})}, \bar{B}\}$. Since $B_0 \leq C$ in Ω , the standard comparison principle concludes our lemma. \square

Remark 3.2 Notice that \bar{B} depends on the parameters in reaction terms. Indeed, direct calculation gives

$$\bar{B} = \frac{1}{k} \left(\frac{r}{z_m l + D} \left(\frac{Q_M - Q_m}{Q_M} \right) \left(\frac{H + I_{in}}{H} \right) - K_{bg} \right)$$

If $\bar{B} > 0$ and B_0 is so small that $B_0 < \bar{B}$, then the uniform bound \bar{B} of B depends on the parameters above. Biological speaking, cyanobacteria blooms depending on environmental, internal factors and its ability to absorb the light. Note that the bound of cyanobacteria is proportional to the difference $Q_M - Q_m$.

Lemma 3.4 Assume that (A_I) and (A_C) . There exists a constant $\bar{p} > 0$ such that the solution to equation $(S_p) - (5)$ satisfies

$$p(x, t) \leq \bar{p} \quad \text{for all } (x, t) \in \bar{\Omega} \times [0, T_{\max}). \quad (13)$$

Proof Lemmas 3.1 and 3.3 conclude the corollary by letting $\bar{p} = Q_M \max\{\|B_0\|_{L^\infty}, \bar{B}\}$. \square

Lemma 3.5 Assume that (A_I) , (A_C) , and P_{in} is bounded. There exists a constant $\bar{P} > 0$ such that the solution to equation $(S_p) - (5)$ satisfies

$$P(x, t) \leq \max\{\|P_0\|_{L^\infty(\Omega)}, \bar{P}\}, \quad \text{for all } (x, t) \in \bar{\Omega} \times [0, T_{\max}). \quad (14)$$

Proof From Equation (4), along with the boundedness of B , the second equation in (S_p) implies that

$$\partial_t P - \beta \Delta P + \beta_P \vec{v}(t) \nabla P = \frac{D}{z_m} (P_h - P) + P_{\text{in}} - \rho(p/B, P)B + lp \quad (15)$$

Let us denote by an operator $\mathcal{L}_3: C^{2,1}(\bar{\Omega} \times (0, T_{\max})) \cap C(\bar{\Omega} \times [0, T_{\max})) \rightarrow C(\bar{\Omega} \times [0, T_{\max}))$, with

$$\begin{aligned} \mathcal{L}_3(P) &= \partial_t P - \beta \Delta P + \beta_P \vec{v}(t) \nabla P - \frac{D}{z_m} (P_h - P) - P_{\text{in}} + \rho(p/B, P)B - lp \\ &\geq -\frac{D}{z_m} (P_h - P) - P_{\text{in}} + \frac{\rho_m \bar{p}}{Q_m} \frac{P}{P + M} - l\bar{p} =: g(P). \end{aligned}$$

Let \bar{P} be a positive zero of g . Note that $g(P) \geq 0$ for all $P \geq \bar{P}$. Since $\mathcal{L}_3(C) \geq 0$ for $C = \max\{\|P_0\|_{L^\infty(\bar{\Omega})}, \bar{P}\}$ and $P_0 \leq C$, the comparison principle shows that (14) holds. \square

Lemmas 3.1, 3.3, 3.5, together with the criterion from Lemma 3.2, we have the following Theorem.

Theorem 3.1 (Global boundedness) *Let $\Omega \subset \mathbb{R}^n$ ($n \geq 1$) be a bounded domain with a smooth boundary. Under Assumptions $(A_f) - (A_c)$, equation $(S_p) - (5)$ has a unique maximal solution $U = (B, p, P) \in C(\bar{\Omega} \times [0, \infty); \mathbb{R}_{\geq 0}^3) \cap C^{2,1}(\bar{\Omega} \times (0, \infty); \mathbb{R}_+^3)$. Furthermore, there exists a constant $C > 0$ independent of t such that*

$$\|B(\cdot, t)\|_{L^\infty} + \|p(\cdot, t)\|_{L^\infty} + \|P(\cdot, t)\|_{L^\infty} \leq C, \quad \forall t \in [0, \infty).$$

3.4 Linear stability analysis around equilibria with small movements

In natural environments, wind plays a significant role in shaping the spatial distribution of cyanobacteria by influencing their transport through air convection. Given that cyanobacteria exhibit minimal random movement, we initially hypothesized that spatial heterogeneity in their distribution could arise due to wind-driven transport. To explore this, we conducted a local stability analysis to assess whether small spatial perturbations around homogeneous steady states could grow over time, potentially leading to the formation of patterns. Our analysis considered a simplified scenario where the wind vector was assumed to be constant, denoted as $\vec{v}(t) = \mathbf{v} = (v_1, v_2) \in \mathbb{R}^2$. Additionally, we assumed that the horizontal transport of cyanobacteria and phosphorus through diffusion and advection was relatively minor compared to their vertical movement, leading to small diffusivity parameters and a small wind-driven transport magnitude $|\mathbf{v}|$. Under these assumptions, we employed first-order perturbation theory to approximate the eigenvalues of the linearized system and determine the stability of the homogeneous steady states.

Our local stability analysis revealed that weak diffusion and wind transport alone are insufficient to sustain long-term spatial heterogeneity. To verify this, we conducted numerical simulations incorporating real wind data. See Figs. 1 and 8. The results showed that while spatial heterogeneity temporarily emerged during the early stages of cyanobacterial bloom, it did not persist over time. Instead, cyanobacteria

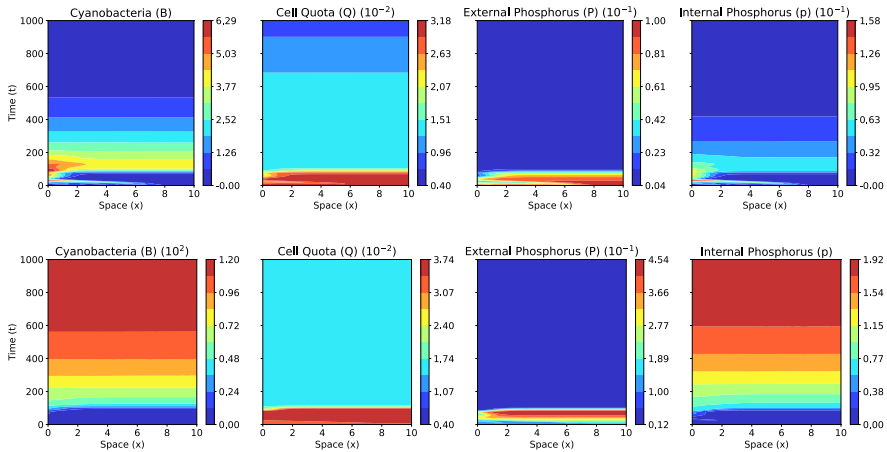


Fig. 1 Time series simulations in one dimension of cyanobacteria, cell quota, and external and intracellular phosphorus over a 1000-day period. The top row represents simulations when $P_h = 0$, and the bottom row when $P_h = 2$. We interpolated a function to a real wind vector from Pigeon Lake, Alberta, in 2023. Once cyanobacteria consume all the initial phosphorus, the respective equilibria remain stable for all time thereafter. For each subfigure, dark blue indicates the lowest cyanobacteria concentration, while green through red indicates progressively higher cyanobacteria concentration, as shown by the colour bars

eventually reached a saturated and spatially uniform state, even under realistic wind conditions. This suggests that the spatial heterogeneity observed in cyanobacterial blooms is primarily a transient phenomenon that occurs only in the initial stages of bloom formation. These findings highlight the importance of temporal dynamics in understanding bloom patterns. While wind-driven transport may influence the early development of spatial heterogeneity, additional mechanisms—such as biological interactions, nutrient availability, or external environmental disturbances—may be required to sustain long-term spatial pattern formation. This motivates further investigation into factors beyond wind-driven transport that could contribute to the persistent spatial structuring of cyanobacterial blooms, such as lake shape and size.

3.4.1 Steady-states without movement

In the case of the homogeneous steady-state, we investigate the steady-state problem of (\mathcal{S}_p)

$$\begin{cases} 0 = U(B, p, P) = rB \left(1 - Q_m \frac{B}{p} \right) h(B) - lB - \frac{D}{z_m} B \\ 0 = V(B, p, P) = \eta(B, p, P) - lp - \frac{D}{z_m} p \\ 0 = W(B, p, P) = \frac{D}{z_m} (P_h - P) - \eta(B, p, P) B + lp. \end{cases} \quad (16)$$

An equivalent system has been studied extensively in works such as Heggerud et al. (2020); Wang et al. (2007) without the term lp on the third equation. To obtain the equivalent system, we simply calculate

$$\frac{dQ}{dt} = \frac{d(V/U)}{dt} = \frac{\eta(B, p, P)}{B} - rQ \left(1 - Q_m \frac{B}{p}\right) h(B) = \rho(Q, P) - rQ \left(1 - \frac{Q_m}{Q}\right) h(B),$$

where Q and $\rho(Q, P)$ are given in the model formulation. The extinction steady state is given by $E_0 = (0, \hat{Q}, P_h)$ such that

$$\begin{aligned} \hat{Q} &= \frac{\tilde{\rho}(P_h)Q_M + rQ_m h(0)}{\tilde{\rho}(P_h) + rh(0)} \\ &= Q_m \frac{rh(0)}{\tilde{\rho}(P_h) + rh(0)} + Q_M \left(1 - \frac{rh(0)}{\tilde{\rho}(P_h) + rh(0)}\right) \text{ with } \tilde{\rho}(P) = \frac{\rho_m}{Q_M - Q_m} \frac{P}{P + M}. \end{aligned}$$

Notice that \hat{Q} is an interpolation between Q_m and Q_M . By Wang et al. (2007), define

$$R_0 = \frac{rh(0)(1 - Q_m/\hat{Q})}{l + D/z_m}.$$

By following the proof of Wang et al. (2007), one can easily check that if $R_0 < 1$, the extinction equilibrium E_0 is globally asymptotically stable for the ODE system even with the term lp . For $R_0 > 1$, E_0 is unstable, and it is easily checked that there exists a positive equilibrium E^* of the system with lp , and cyanobacteria uniformly persist. Note that when $P_h = 0$, $\hat{Q} = Q_m$, the extinction equilibrium E_0 is globally asymptotically stable since $R_0 = 0$. Therefore, the positiveness of P_h is necessary for cyanobacteria to persist uniformly.

3.4.2 Steady-states with small diffusion and constant advection

By abusing the notation, let $E_0 = (0, 0, P_h)$ and $E^* = (B^*, p^*, P^*)$ be the extinction and the positive constant equilibrium of the (B, p, P) system (\mathcal{S}_p), respectively. Here we calculate $p^* = B^*Q^*$ based on the (B, Q, P) system of ODEs. However, if the term p/B appears in the evaluation of E_0 , we use \hat{Q} instead. Specifically, we assume that if $E = (B, p, P)$ approaches E_0 as $t \rightarrow \infty$, then p/B converges to \hat{Q} in the same limit. We linearize system (\mathcal{S}_p) at $\bar{E} = (\bar{B}, \bar{p}, \bar{P})$, where \bar{B} , \bar{p} , and \bar{P} are nonnegative constants. Let $\tilde{E} = E - \bar{E}$, and dropping the tilde signs for notational simplicity. Inspired by the transformation described in Cantrell and Cosner (2004), let

$$B(x, t) = \sum_n \hat{B}(t)e^{inx}, \quad p(x, t) = \sum_n \hat{p}(t)e^{inx}, \quad P(x, t) = \sum_n \hat{P}(t)e^{inx}, \quad (17)$$

where n is a mode number that determines the spatial frequency of perturbations.

We obtain the transformed system

$$\begin{aligned}
 \hat{B}_t &= -\alpha n^2 \hat{B} - \beta_B v i n \hat{B} + r \left(1 - \frac{2Q_m \bar{B}}{\bar{p}} \right) h(\bar{B}) \hat{B} + r \left(1 - \frac{Q_m \bar{B}}{\bar{p}} \right) h'(\bar{B}) \bar{B} \hat{B} \\
 &\quad + r \frac{Q_m \bar{B}^2}{\bar{p}^2} h(\bar{B}) \hat{p} - l \hat{B} - \frac{D}{z_m} \hat{B}, \\
 \hat{p}_t &= -\alpha n^2 \hat{p} - \beta_B v i n \hat{p} + \rho_m \frac{Q_M}{Q_M - Q_m} \frac{\bar{P}}{\bar{P} + M} \hat{B} - \frac{\rho_m}{Q_M - Q_m} \frac{\bar{P}}{\bar{P} + M} \hat{p} \\
 &\quad + \rho_m \frac{Q_M \bar{B} - \bar{p}}{Q_M - Q_m} \frac{M}{(\bar{P} + M)^2} \hat{P} \\
 &\quad - l \hat{p} - \frac{D}{z_m} \hat{p}, \\
 \hat{P}_t &= -\beta n^2 \hat{P} - \beta_P v i n \hat{P} - \frac{D}{z_m} \hat{P} - \rho_m \frac{Q_M}{Q_M - Q_m} \frac{\bar{P}}{\bar{P} + M} \hat{B} + \frac{\rho_m}{Q_M - Q_m} \frac{\bar{P}}{\bar{P} + M} \hat{p} \\
 &\quad - \rho_m \frac{Q_M \bar{B} - \bar{p}}{Q_M - Q_m} \frac{M}{(\bar{P} + M)^2} \hat{P} + l \hat{P},
 \end{aligned} \tag{18}$$

Further, the entries of the Jacobian matrix of the transformed equation are given by

$$\begin{aligned}
 a_{11} &= -\alpha n^2 - \beta_B v i n - l - \frac{D}{z_m} + r \left(1 - \frac{2Q_m \bar{B}}{\bar{p}} \right) h(\bar{B}) + r \left(1 - \frac{Q_m \bar{B}}{\bar{p}} \right) h'(\bar{B}) \bar{B}, \\
 a_{12} &= r \frac{Q_m \bar{B}^2}{\bar{p}^2} h(\bar{B}), \\
 a_{21} &= \rho_m \frac{Q_M}{Q_M - Q_m} \frac{\bar{P}}{\bar{P} + M}, \\
 a_{22} &= -\alpha n^2 - \beta_B v i n - l - \frac{D}{z_m} - \frac{\rho_m}{Q_M - Q_m} \frac{\bar{P}}{\bar{P} + M}, \\
 a_{23} &= \rho_m \frac{Q_M \bar{B} - \bar{p}}{Q_M - Q_m} \frac{M}{(\bar{P} + M)^2}, \\
 a_{31} &= -\rho_m \frac{Q_M}{Q_M - Q_m} \frac{\bar{P}}{\bar{P} + M} = -a_{21}, \\
 a_{32} &= \frac{\rho_m}{Q_M - Q_m} \frac{\bar{P}}{\bar{P} + M} + l, \\
 a_{33} &= -\beta n^2 - \beta_P v i n - \frac{D}{z_m} - \rho_m \frac{Q_M \bar{B} - \bar{p}}{Q_M - Q_m} \frac{M}{(\bar{P} + M)^2}.
 \end{aligned}$$

The Jacobian matrix $J = (a_{ij})$ is also of the form

$$J = A + \Delta,$$

where A is a matrix with $n = 0$ and $\Delta = -n^2 \text{diag}(\alpha, \alpha, \beta) - i n \text{diag}(\beta_B, \beta_B, \beta_P)$ with small positive parameters α, β, β_B , and β_P . The imaginary unit is denoted by i , and n is a natural number. In this regard, we can think of J as a perturbation of A with a small matrix Δ , say $\|\Delta\| \ll \|A\|$. Then the eigenvalues of J can be approximately analyzed using the first-order perturbation theory. Assume that the perturbed eigenvalue μ_i and eigenvector u_i can be expressed as $\mu_i = \lambda_i + \epsilon_i$ and $u_i = v_i + w_i$,

where ϵ_i and w_i represent small first-order corrections. Substituting these into the eigenvalue equation $Ju_i = \mu_i u_i$ leads to

$$(A + \Delta)(v_i + w_i) = (\lambda_i + \epsilon_i)(v_i + w_i).$$

Expanding both sides gives

$$Av_i + Aw_i + \Delta v_i + \Delta w_i = \lambda_i v_i + \lambda_i w_i + \epsilon_i v_i + \epsilon_i w_i.$$

Subtracting $Av_i = \lambda_i v_i$ from both sides results in

$$Aw_i + \Delta v_i + \Delta w_i = \lambda_i w_i + \epsilon_i v_i + \epsilon_i w_i.$$

Since Δw_i and $\epsilon_i w_i$ are second-order small terms, they can be ignored, simplifying to

$$Aw_i + \Delta v_i \approx \lambda_i w_i + \epsilon_i v_i.$$

Rearranging yields

$$(A - \lambda_i I)w_i \approx -\Delta v_i + \epsilon_i v_i.$$

Taking the inner product with v_i gives

$$v_i^*(A - \lambda_i I)w_i \approx -v_i^* \Delta v_i + \epsilon_i v_i^* v_i.$$

Since $(A - \lambda_i I)w_i$ is orthogonal to v_i , the left-hand side vanishes. With $v_i^* v_i = 1$, this simplifies to

$$\epsilon_i \approx v_i^* \Delta v_i.$$

Thus, the first-order corrected eigenvalue is

$$\mu_i \approx \lambda_i + v_i^* \Delta v_i.$$

For a diagonal perturbation matrix $\Delta = \text{diag}(d_1, d_2, d_3)$, this simplifies to

$$v_i^* \Delta v_i = d_1 |v_{i1}|^2 + d_2 |v_{i2}|^2 + d_3 |v_{i3}|^2,$$

where $|v_{ik}|^2$ represents the squared magnitude of the k -th component of v_i .

For the given problem, the perturbation terms are defined as

$$d_1 = d_2 = -n^2 \alpha - in\beta_B, \quad d_3 = -n^2 \beta - in\beta_P.$$

Thus, the correction becomes

$$\epsilon_i = -n^2 (\alpha(|v_{i1}|^2 + |v_{i2}|^2) + \beta|v_{i3}|^2) - in (\beta_B(|v_{i1}|^2 + |v_{i2}|^2) + \beta_P|v_{i3}|^2).$$

Therefore, the first-order corrected eigenvalues of J are

$$\mu_i \approx \lambda_i - n^2 (\alpha(|v_{i1}|^2 + |v_{i2}|^2) + \beta|v_{i3}|^2) - in (\beta_B(|v_{i1}|^2 + |v_{i2}|^2) + \beta_P|v_{i3}|^2)$$

where $|v_{ij}|^2$ represents the squared magnitude of the j th component of the eigenvector v_i associated with A . As a result, eigenvalues of J can be approximated as

$$\begin{aligned} \operatorname{Re}(\mu_i) &\approx \operatorname{Re}(\lambda_i) - n^2(\alpha v_{i1}^2 + \alpha v_{i2}^2 + \beta v_{i3}^2) \quad \text{and} \\ \operatorname{Im}(\mu_i) &\approx \operatorname{Im}(\lambda_i) - n(\beta_B v_{i1}^2 + \beta_B v_{i2}^2 + \beta_P v_{i3}^2). \end{aligned} \quad (19)$$

Note that the approximation (19) for the eigenvalues is only valid when the perturbation is relatively small. It is unclear whether the derived formula for the eigenvalues μ_i remains accurate for large values of the parameters α, β_B, β_P . To validate the analytical eigenvalue formula with the large values of parameters associated with diffusion and advection, we compare it with the numerical eigenvalues of the Jacobian matrix J , calculated using parameter values informed by real data. Since it is difficult to determine the positive equilibrium E^* analytically, we first numerically compute the exact value of E^* from the ODE system (16). In our MATLAB simulations, we use the following parameter values: $\alpha = 0.01, \beta = 0.02, \beta_B = 0.05, \beta_P = 0.075, z_m = 5, Q_m = 0.004, Q_M = 0.04, K_{bg} = 0.3, k = 0.0004, I_{in} = 300, H = 120, l = 0.35, D = 0.02, \rho_m = 1, M = 1.5$. We then vary the parameters r and P_h to examine different scenarios:

- (1) We compute the numerical eigenvalues of $J = (a_{ij})$ near the extinction equilibrium $E_0 = (0, 0, P_h)$, taking $r = 0.7$ and $P_h = 0$, so that $R_0 = 0$. In this case, the extinction equilibrium is expected to be stable. Indeed, we observe that all eigenvalues have negative real parts for all n , confirming the stability of E_0 . See Fig. 2.
- (2) Numerical eigenvalues of $J = (a_{ij})$ around $E_0 = (0, 0, P_h)$ when $r = 0.7$ and $P_h = 0.2$, so $R_0 = 0.9494$. See Fig. 3.

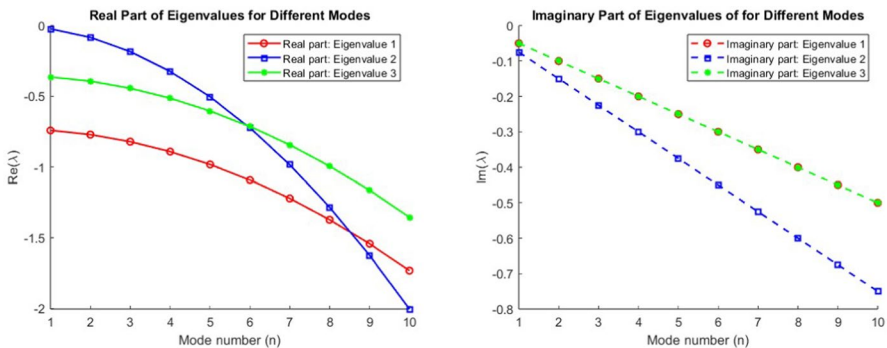


Fig. 2 Real and imaginary part of eigenvalues for different modes for the extinction equilibrium E_0 , respectively. Here we set $r = 0.7$ and $P_h = 0$

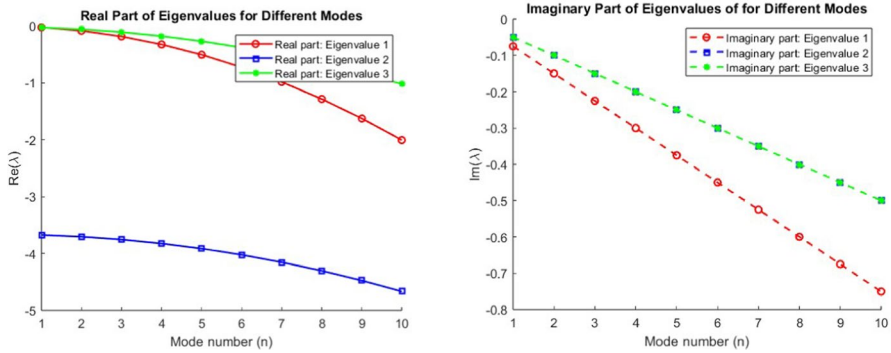


Fig. 3 Real and imaginary part of eigenvalues of J for different modes for the extinction equilibrium E_0 , respectively. $r = 0.7$ and $P_h = 0.2$

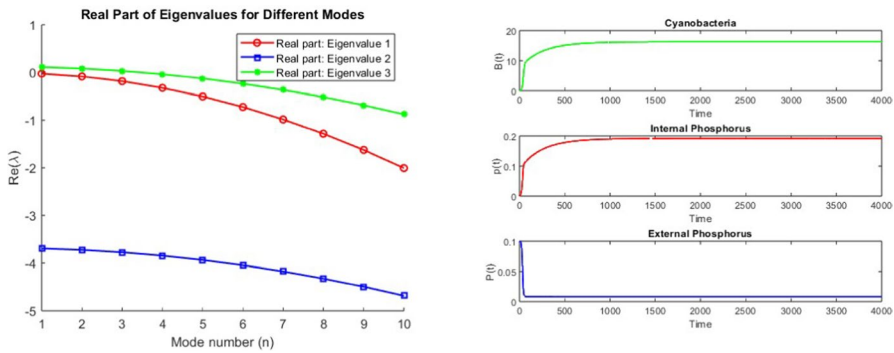


Fig. 4 The left figure represents the real part of eigenvalues of J for different modes for the positive equilibrium E_0 when $r = 1$ and $P_h = 0.2$. The third eigenvalue of J around E_0 is positive for $n = 1, 2$, and 3 . With the same parameter, the right figure illustrates the solution of ODE system for (S_p) . The solution at time 4000 is considered to be the equilibrium $E^* := (16.2785, 0.1920, 0.0080)$

- (3) Numerical eigenvalues of $J = (a_{ij})$ around $E_0 = (0, 0, P_h)$ and $E^* = (B^*, p^*, P^*)$ when $r = 1$, $P_h = 0.2$ and $R_0 = 1.3497 > 1$. In this case, E_0 is linearly unstable, and there is a positive linearly stable equilibrium $E^* = (16.2785, 0.1920, 0.0080)$, which is computed by a numerical simulation of the ODE system for (S_p) . See Figs. 4 and 5.

We have observed the linear stability of the extinction equilibrium E_0 and the positive equilibrium E^* numerically. As we found in the first-order perturbation theory, the result for the real part of the numerical eigenvalues is a decreasing quadratic polynomial in terms of n , which implies that a small diffusion of individuals ultimately stabilizes our system. Therefore, the result implies that the small random movement of cyanobacteria in lakes and minor horizontal movement caused by wind contribute to stabilizing the overall system.

These results lead us to the following question: What factors drive the spatial patterns of cyanobacteria observed in lakes? Since the random movement of cyano-

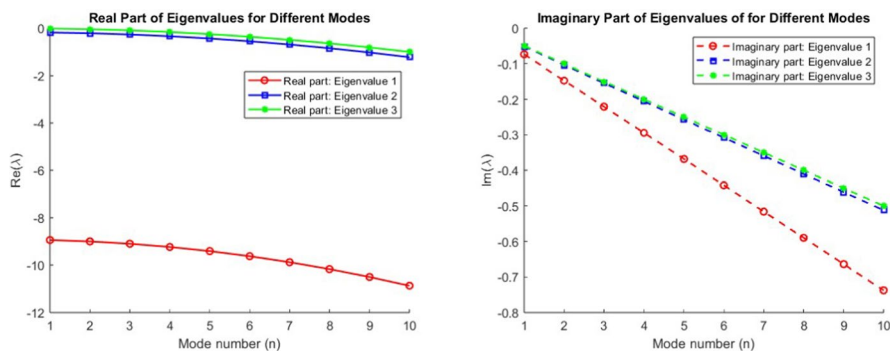


Fig. 5 Real and imaginary part of eigenvalues of J for different modes around the positive equilibrium $E^* = (16.2785, 0.1920, 0.0080)$, respectively. $r = 1$ and $P_h = 0.2$

bacteria is generally small, we can consider several possible factors: (1) Movement induced by lake wind. Unlike the mathematical analysis we performed, the strength and direction of the wind vary spatially and change over time. As a result, heterogeneous changes in currents may influence the spatial patterns over a large time. (2) Variations in vertical exchange across space - Even within a lake, convective processes and water depth differ across locations, leading to variations in the amount of vertical exchange.

3.5 Possibility of long-term spatial heterogeneity

In the model (\mathcal{S}_p), each coefficient encapsulates key physical, chemical, and biological processes that influence the spatial heterogeneity of cyanobacterial biomass and nutrient concentrations in natural lakes. For instance, the diffusion terms $\alpha\Delta B$, $\alpha\Delta p$, and $\beta\Delta P$ represent mixing driven by molecular and turbulent diffusion, where the coefficients α and β may vary spatially depending on lake bathymetry, stratification strength, and local turbulence. Similarly, the advection terms involving the velocity field $\vec{v}(t)$ capture the directional transport of substances via wind-driven surface flows.

Moreover, the vertical exchange terms, expressed as D, z_m , describe the mixing between surface and deeper layers and are modulated by both the mixing coefficient D and the epilimnion depth z_m , both of which are strongly location-dependent in stratified lakes. Given the spatial variability of environmental drivers such as light, oxygen, nutrient availability, and physical disturbance, it is natural and ecologically relevant to consider spatially heterogeneous coefficients (e.g., $\alpha(x)$, $\beta(x)$, $D(x)$, $z_m(x)$) in order to capture better realistic dynamics observed in field conditions.

Despite analyzing numerical simulations of the associated ODE system with different diffusivity, we were unable to identify any signature of Turing-type pattern formation in this model. Specifically, the positive stable equilibrium E^* of the spatially homogeneous ODE system remained stable even as the diffusive modes were introduced with large difference between α and β , and no diffusion-driven instability was observed. This is supported by Fig. 6, where the real part of eigenvalues for

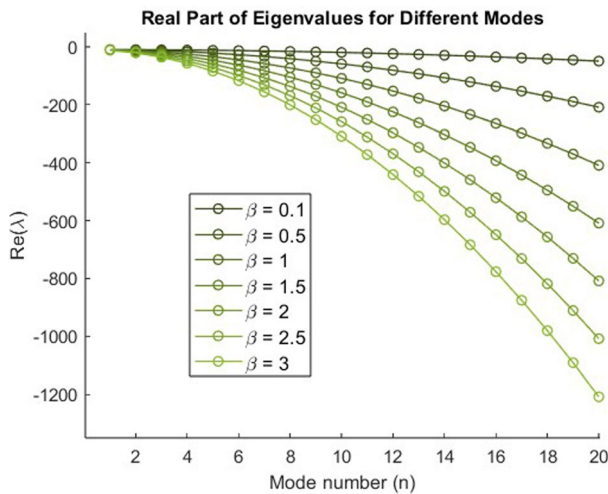


Fig. 6 Real parts of the dominant eigenvalues for Fourier modes $n = 1, \dots, 20$ around the positive equilibrium $E^* = (16.2785, 0.1920, 0.0080)$, computed for varying values of the parameter β , provided $\alpha = 0.1$. All other parameters were taken as in Fig. 5. Each curve corresponds to a different β value. Increasing β leads to more negative eigenvalues for higher modes, indicating enhanced damping of spatial perturbations

increasing β (with fixed $\alpha = 0.1$) show monotonic decay in the real parts, indicating enhanced stability rather than pattern formation.

Furthermore, spatially heterogeneous coefficients in the diffusion terms, such as $\alpha(x)$ or $\beta(x)$, are insufficient to sustain long-term heterogeneity. This is because each component B , p , and P should follow the Fickian-type diffusion, which corresponds to Brownian motion and naturally leads to spatial homogenization over time. Since cyanobacteria and nutrient particles do not exhibit any cognitive movement, they simply follow classical Fickian diffusion.

To overcome this limitation, we next investigate whether spatial heterogeneity in the vertical exchange parameters, specifically in the vertical exchange parameter $D(x)$ and the depth of the epilimnion $z_m(x)$ for $x \in \Omega \subset \mathbb{R}^2$, can lead to pattern formation. We observe long-term spatially heterogeneous distribution by carrying out numerical simulations with the nonuniform coefficients D and z_m over two dimensional rectangular domain. We take z_m and D with smooth, radially varying functions such that the virtual lake resembles a shallow rimmed, deeper centre basin. For grid coordinates $(x, y) \in [0, L_x] \times [0, L_y]$ we set

$$r(x, y) = \frac{\sqrt{(x - L_x/2)^2 + (y - L_y/2)^2}}{0.5\sqrt{L_x^2 + L_y^2}},$$

and

$$z_m(x, y) = z_{\min} + (z_{\max} - z_{\min})[1 - r(x, y)^2],$$

$$D(x, y) = D_{\min} + (D_{\max} - D_{\min})[1 - r(x, y)^2].$$

The ranges are $1 < z_m(x, y) < 8$, and $0.0005 < D(x, y) < 0.5$. For the initial conditions, cyanobacteria is defined with three Gaussian distributions centred at $(x, y) = (L_x/4, L_y/4)$, $(L_x/2, L_y/2)$, $(3L_x/4, 3L_y/4)$:

$$\tilde{B}_0(x) = \exp\left[-\frac{(x-\frac{L}{4})^2 + (y-\frac{L}{4})^2}{2\sigma_1^2}\right] + \exp\left[-\frac{(x-\frac{L}{2})^2 + (y-\frac{L}{2})^2}{2\sigma_2^2}\right] + \exp\left[-\frac{(x-\frac{3L}{4})^2 + (y-\frac{3L}{4})^2}{2\sigma_3^2}\right],$$

$$\sigma_1 = \frac{L}{20}, \sigma_2 = \frac{L}{30}, \sigma_3 = \frac{L}{15}.$$

The profile is normalized such that $B_0(x, y) = \tilde{B}_0(x, y)/\|\tilde{B}_0\|_{L^\infty}$. The initial cell-quota field is spatially uniform, $Q_0(x, y) \equiv Q_m$, while dissolved phosphorus is set to a low background level, $P_0(x, y) \equiv 0.10$ mg P/m². Internal phosphorus then satisfies $p_0(x, y) = B_0(x, y) Q_0(x, y)$. Unlike the homogeneous cases, these simulations result in spatially heterogeneous distribution on the domain. As shown in Fig. 7, the bottom row displays localized concentration zones near the domain boundary, especially for cyanobacteria and internal phosphorus, highlighting the potential role of heterogeneous vertical dynamics in sustaining nonuniform spatial states.

This investigation on long-term spatial heterogeneity in our model shows that spatial variation in vertical mixing can play an important role in shaping how cyanobacteria and nutrients are distributed in lakes. We found that even without classical Turing-type instabilities, steady and uneven spatial patterns can still appear when vertical exchange rate and depth of epilimnion vary across space. This suggests that the patchy distributions of cyanobacteria often seen in real lakes may not only be caused by biological interactions or external disturbances, but can also come from

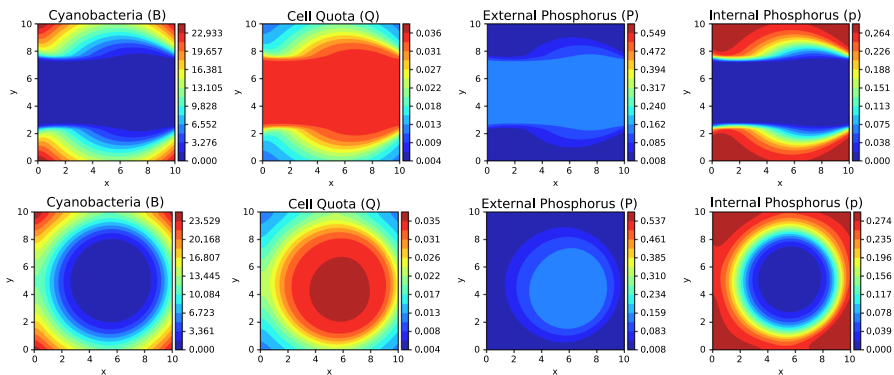


Fig. 7 A fixed window of a time series simulation in two dimensions of cyanobacteria, cell quota, and external and intracellular phosphorus at 1000-days. The top row represents simulations with a constant wind vector, and the bottom row with a function interpolated to a real wind vector from Pigeon Lake, Alberta, in 2023. The water-column depth and vertical exchange vary smoothly in the plane, mimicking a dish-shaped basin with the hypolimnion at its centre. For simplicity, we chose a radially symmetric, continuously differentiable profile that keeps depth and exchange minimal at the shoreline, peaks smoothly at the centre, and preserves convenience for the finite-difference scheme. Full details of the equations used for spatially-dependent parameters can be found in our GitHub repository

the spatial structure of physical transport processes. Therefore, including realistic spatial heterogeneity in coefficients of our system is crucial for better understanding the behaviour of shallow aquatic ecosystems.

3.6 Time series simulations

In this section, we conduct numerical simulations of system (S_p) with the addition of Q . We will observe the dynamics of our state variables in both short and long-term timescales. We consider discrete diffusion and advection in space. All simulations were performed in Python. Details can be found in Appendix A. We consider one- and two-dimensional spatial domains $x \in [0, L]$ and $(x, y) \in [0, L_x] \times [0, L_y]$, respectively, of model (S_p) with the addition of Q . We impose homogeneous Neumann boundary conditions. The parameters and functions are as described in the model formulation. Using the finite difference method, we discretize the spatial domain and for any spatially dependent variable $U(x, t)$, let $U_i(t) \approx U(x_i, t)$. The first- and second-order spatial derivatives are approximated by central difference schemes, except advection, which is approximated by an upwind scheme. This described discretization transforms the system into a system of ODEs in time for the arrays $B_i(t)$, $Q_i(t)$, $P_i(t)$, and $p_i(t)$. We then integrate the resulting ODE system in time using the BDF method built into Python. Specifically, we observe short (transient) and medium timescales in Figs. 8, 11 and 12. To observe the asymptotic dynamics of our model, we also ran the simulations for 1000 days in Figs. 1 and 7.

In addition to the one-dimensional simulations, we numerically solved (S_p) on a realistic lake-shaped domain using the Firedrake package to perform finite element method (FEM) simulations (Ham 2023). Specifically, we rendered a closed curve of the boundary of Pigeon Lake, Alberta, Canada, from Geographic Information Systems (GIS) lake shape provided by the government of Alberta ([1]) and then generated an unstructured triangular mesh of approximately 5000 elements spanning this

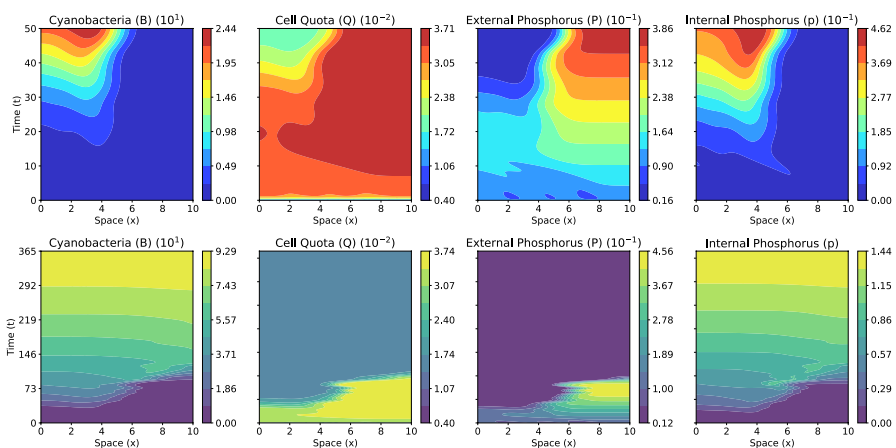


Fig. 8 Time series simulations in one dimension of cyanobacteria, cell quota, external and intracellular phosphorus over short (50 days) and long (365 days) time periods. We interpolated a function to a real wind vector from Pigeon Lake, Alberta, in 2023

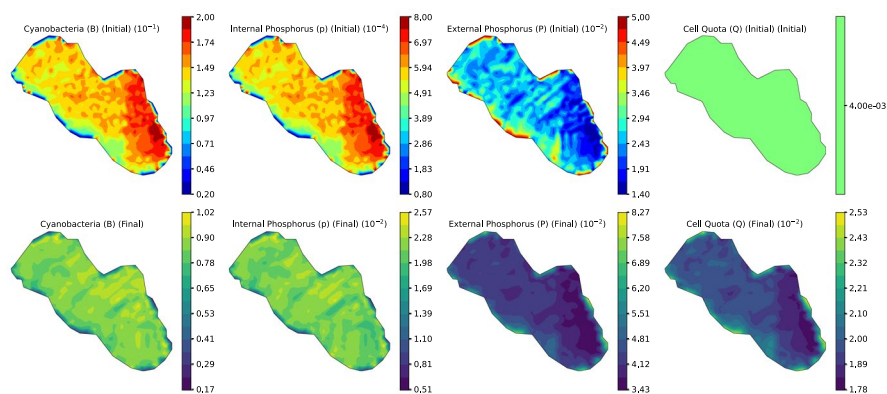


Fig. 9 Time series simulations in two dimensions of cyanobacteria, cell quota, external and internal phosphorus from August 6, 2023 to August 27, 2023. We interpolated a function to a real wind vector from Pigeon Lake, Alberta and used Sentinel-2 data for the initial condition of cyanobacteria. We used the FEM and GIS data to simulate the system on a realistic lake domain

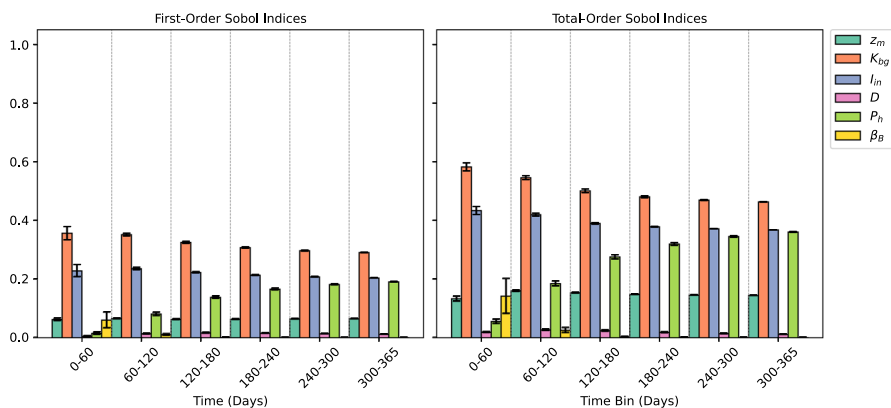


Fig. 10 Global sensitivity analysis using first- and total-order Sobol indices to compare the impact of physical lake conditions on the growth of cyanobacteria over space and time. The simulation is for 365 days, with contributions binned into ~ 60 day intervals. We interpolated a function to a real wind vector from Pigeon Lake, Alberta, in 2023

domain. The parameters are identical to those of the one-dimensional simulations, and advection is represented by a time-dependent wind vector derived from local meteorological data in 2023, which we then interpolated. We updated $\vec{v}(t)$ accordingly for each time step to capture wind-driven surface mixing. For improved realism, we use a cyanobacteria estimation (CE) obtained from Sentinel-2 (Zambrano-Luna et al. 2025) for our initial conditions and model validation, shown in Figs. 9 and 17. Notably, after simulating the model from August 6, 2023, to August 27, 2023, we obtained a Root Mean Square Error (RMSE) of 0.121 and a Pearson R coefficient of 0.857, which measures the linear relationship between simulated and observed values. The details can be found in Appendix A.2. We set the initial condition for dissolved phosphorus to be lower in areas of high cyanobacteria concentration due

to the assumed local consumption, with added random noise. The FEM implementation follows our weak formulation from Appendix A.2, discretizing the domain with Galerkin polynomials for B , p , P , and Q . As shown in Fig. 9, the distribution of cyanobacteria evolves in spatially heterogeneous ways.

3.7 Sobol indices

We performed a global sensitivity analysis to investigate how our model's physical lake condition parameters influence cyanobacterial biomass predictions over the simulated time window (Fig. 10). In particular, we assessed the relative importance of the following parameters: epilimnion depth (z_m), background light attenuation (K_{bg}), water exchange rate (D), external phosphorus input (P_h), and the cyanobacterial advection coefficient (β_B). We utilized Sobol's method (Sobol 2001), which employs Monte Carlo sampling to assess the contributions of individual factors and their interactions in generating the overall variability in the cyanobacteria solution. Sobol's method provides two indices: the first-order Sobol index $S1_f$, which measures how much of the output variance is attributable to a factor f alone, and the total-order Sobol index ST_f , which captures both the direct effect of f and all its interactions with the other parameters. Further details can be found in Appendix A.

4 Discussion

Cyanobacterial blooms (CBs), resulting from complex interactions between nutrient availability and physical lake characteristics, are responsible for numerous economic and environmental problems, including biodiversity loss and water contamination (Paerl and Otten 2013). In this paper, cyanobacteria take nutrients from the surrounding water and modulate their intracellular phosphorus quota under varying light conditions, thereby influencing their growth and spatial distribution. To better understand these dynamics, we developed a reaction-diffusion–advection model that integrates ecological stoichiometry with realistic wind conditions. This methodology enabled us to rigorously characterize how heterogeneity in nutrient inputs and water movement impacts bloom formation and persistence. Theoretical outcomes show that model (\mathcal{S}_p) behaves well both mathematically and biologically. According to the results in Sect. 3 and corresponding remarks, some critical thresholds for CBs are rigorously derived. Specifically, we examine the basic ecological reproductive indices of cyanobacteria (see Sect. 3) through various transformations and classical theoretical techniques.

After approximately 300 days, each system—no movement, synthetic wind, and real data-driven wind—displays qualitatively similar behaviour for each set of one-dimensional simulations. This phenomenon occurs despite heterogeneous initial conditions because cyanobacteria eventually either saturate the available space during a bloom or become extinct. Notably, while differences in the magnitude of external phosphorus are evident across the movement-based simulations, the extreme values of cyanobacteria concentration, intracellular phosphorus, and thus cell quota remain relatively consistent. In other words, once the cyanobacterial population exceeds a

critical threshold, advective and diffusive movement exerts a diminished influence on overall dynamics (Huisman and Weissing 1994; Paerl and Huisman 2008). Our two-dimensional simulations on a lake-shaped domain show the complex interactions of local land geometry, wind-driven advection, and nutrient stoichiometry related to CBs. The irregular boundary geometry produces concentration hot spots along sharply curving shorelines (Fig. 9). This phenomenon partially corroborates earlier one-dimensional findings, once a critical threshold of dissolved phosphorus is met, strong gradients in cyanobacteria emerge, particularly where wind currents stagnate or recirculate. From a water-resource management perspective, these spatially explicit results highlight the importance of controlling inflow nutrients in shallow or sheltered segments of the lake boundary, where wind-driven advection may be insufficient to dilute bloom-prone regions.

To further investigate the steady-state behaviour of our model, we simulated the system for 1000 days using a finite difference scheme (Fig. 1). When $P_h = C > 0$, after the cyanobacteria deplete the initial phosphorus supply, the model settles into an internally maintained constant steady state that is asymptotically stable for all future time (Fig. 1). Conversely, if $P_h = 0$, once the phosphorus is exhausted, the extinction equilibrium is reached and remains stable. In dynamical systems terms, $P_h = 0$ represents a bifurcation point, marking a qualitative change in the system's long-term behaviour. These outcomes are consistent across all simulation scenarios and align with the analysis presented in Sect. 3.4. These results highlight the need to monitor nutrient inputs from anthropogenic sources closely (Zhang et al. 2022; Zhao and Huang 2014; Paerl and Otten 2013). The results of the FEM simulations demonstrate that our spatial model can faithfully reproduce the short-term evolution of bloom hotspots. After the 21-day window, simulated CE fields matched Sentinel-2 observations with an RMSE of 0.121 and a Pearson's correlation coefficient of 0.857, correctly capturing both the emergence and dispersal of high-intensity patches. These numerical figures highlight the model's potential for future development in operational forecasting and its ability to inform targeted sampling and management actions in real-time.

In addition to the early patchy distribution, we also investigated the possibility of long-term spatial heterogeneity with our model by incorporating spatially nonuniform coefficients, the vertical exchange rate D and the depth of epilimnion z_m . The resulting spatial distributions showed persistent non-uniformity over time, despite the absence of any possibility of Turing-like pattern. These findings emphasize that environmental heterogeneity can shape spatial organization and must be carefully considered when developing predictive models of bloom dynamics. Furthermore, they highlight the importance of incorporating realistic spatial variability in future modelling efforts to improve ecological forecasts and management strategies.

Our global sensitivity analysis, implemented via Sobol indices (Sobol 2001; Herman and Usher 2017), reveals that light attenuation and intensity consistently domi-

nate cyanobacterial growth. In contrast, epilimnion depth and water exchange rate exert a relatively constant yet minor influence over the simulation period. Interestingly, the relative impact of input phosphorus becomes more pronounced over time. This trend resonates with previous observational and modelling studies (Gao et al. 2020; Du et al. 2022; Reynolds 2006). Moreover, the advection coefficient proves to be significantly more influential when the model incorporates real wind data than when using an idealized oscillatory wind function. This is likely due to the spatial symmetry induced by the sinusoidal forcing, which tends to homogenize the initial conditions before bloom formation (Cao et al. 2006; Huisman et al. 2018). Overall, these findings reinforce the dominant role of light and nutrient dynamics in bloom development and highlight the importance of incorporating realistic physical forcing in future modelling efforts (Qin et al. 2009; Paerl and Huisman 2008).

In model (\mathcal{S}_p), we omit a grazing compartment and many other lake-specific forcings. We recognize that real-world heterogeneity stems from various complex drivers, including wind-driven surface currents, seiches, seasonal stratification, depth-dependent light gradients, nutrient hotspots near tributaries or anoxic sediments, species-specific buoyancy regulation, zooplankton grazing refugia, short-lived meteorological pulses, and anthropogenic disturbances. Incorporating all of these processes into a single framework would inhibit the analytical clarity that motivates our study. Therefore, we present a mechanistic baseline: a horizontally explicit reaction-diffusion-advection system that couples ecological stoichiometry with the simplest physically justified transport terms. This baseline already recovers key phenomena such as spatial patchiness driven by shear, shoreline amplification under irregular bathymetry, and parameter-controlled extinction or bloom persistence, while remaining analytically tractable. Future extensions could embed a depth-resolved column or a 3D hydrodynamic layer to capture vertical migration and internal loading, adding a grazer state to explore how spatial refuges influence toxin transfer through the food web, or impose spatially heterogeneous source terms to mimic point-source nutrient inflows.

The explicit calculation of the internal steady state could benefit scientists and policymakers by providing precise guidelines for the quantity of cyanobacteria, given the different parameter values. Most existing reaction-diffusion models incorporating nutrient stoichiometry via a Droop formulation focus on diffusion in one-dimensional space, with limited consideration of reaction terms beyond growth (Hsu et al. 2010, 2014, 2017). By contrast, our work integrates wind-driven advection and nutrient stoichiometry in a two-dimensional setting to capture more realistic bloom dynamics. This approach provides a better understanding of how environmental forcing and boundary geometry interact to shape CBs, offering insights that can inform future research and resource management strategies.

Appendix A: Numerical supplementation

Appendix A.1: Finite difference method

The one-dimensional version of model (\mathcal{S}_p) is given by

$$\begin{aligned}\frac{\partial B}{\partial t} &= \alpha \frac{\partial^2 B}{\partial x^2} - \beta_B v(t) \frac{\partial B}{\partial x} + rB \left(1 - \frac{Q_m}{Q}\right) h(B) - lB - \frac{D}{z_m} B, \\ \frac{\partial Q}{\partial t} &= \alpha \frac{\partial^2 Q}{\partial x^2} + \left(2\alpha \frac{\partial B / \partial x}{B} - \beta_B v(t)\right) \frac{\partial Q}{\partial x} + \rho(Q, P) - rQ \left(1 - \frac{Q_m}{Q}\right) h(B), \\ \frac{\partial P}{\partial t} &= \beta \frac{\partial^2 P}{\partial x^2} - \beta_P v(t) \frac{\partial P}{\partial x} + \frac{D}{z_m} (P_h - P) - \rho(Q, P) B + lQB, \\ \frac{\partial p}{\partial t} &= \alpha \frac{\partial^2 p}{\partial x^2} - \beta_B v(t) \frac{\partial p}{\partial x} + \eta(B, p, P) - lp - \frac{D}{z_m} p.\end{aligned}\quad (20)$$

We impose Neumann boundary conditions at $x = 0$ and $x = L$:

$$\frac{\partial B}{\partial x} = \frac{\partial Q}{\partial x} = \frac{\partial P}{\partial x} = \frac{\partial p}{\partial x} = 0 \quad \text{at } x = 0, L. \quad (21)$$

Using the finite difference method, we discretize the spatial domain into N_x uniform grid points, where

$$x_i = i\Delta x, \quad i = 0, 1, \dots, N_x - 1, \quad \text{where } \Delta x = \frac{L}{N_x - 1}.$$

For any spatially dependent variable $U(x, t)$, let $U_i(t) \approx U(x_i, t)$. The second-order spatial derivatives are approximated by second-order central differences

$$\frac{\partial^2 U}{\partial x^2}(x_i, t) \approx \frac{U_{i+1}(t) - 2U_i(t) + U_{i-1}(t)}{\Delta x^2}.$$

First-order spatial derivatives are approximated by a second-order central difference

$$\frac{\partial U}{\partial x}(x_i, t) \approx \frac{U_{i+1}(t) - U_{i-1}(t)}{2\Delta x}.$$

At the boundaries ($i = 0$ and $i = N_x - 1$), we apply the Neumann conditions

$$\frac{\partial U}{\partial x}(x_0, t) \approx \frac{U_1(t) - U_0(t)}{\Delta x} = 0 \implies U_1(t) = U_0(t),$$

and similarly at x_{N_x-1}

$$\frac{\partial U}{\partial x}(x_{N_x-1}, t) \approx \frac{U_{N_x-1}(t) - U_{N_x-2}(t)}{\Delta x} = 0 \implies U_{N_x-1}(t) = U_{N_x-2}(t).$$

This discretization transforms the PDE system into a system of ODEs in time for the arrays $B_i(t)$, $Q_i(t)$, $P_i(t)$, and $p_i(t)$. We then integrate the resulting ODE system in time using the BDF method built into Python. For the initial conditions, cyanobacteria is defined with three Gaussian distributions centred at $x = L/4$, $L/2$, $3L/4$:

$$\tilde{B}_0(x) = \exp\left[-\frac{(x-\frac{L}{4})^2}{2\sigma_1^2}\right] + \exp\left[-\frac{(x-\frac{L}{2})^2}{2\sigma_2^2}\right] + \exp\left[-\frac{(x-\frac{3L}{4})^2}{2\sigma_3^2}\right], \quad \sigma_1 = \frac{L}{20}, \quad \sigma_2 = \frac{L}{30}, \quad \sigma_3 = \frac{L}{15}.$$

The profile is normalized such that

$$B_0(x) = \frac{\tilde{B}_0(x)}{\max_{x \in [0, L]} \tilde{B}_0(x)}.$$

The initial cell-quota field is spatially uniform, $Q_0(x) \equiv Q_m$, while dissolved phosphorus is set to a low background level, $P_0(x) \equiv 0.10 \text{ mg P m}^{-2}$. Internal phosphorus then satisfies $p_0(x) = B_0(x) Q_0(x)$. The 2D finite difference scheme is defined similarly.

Appendix A.2: Two-dimensional finite elements method

Here, we detail the derivation of the weak formulation for our stoichiometric PDE system (\mathcal{S}_p) on a two-dimensional lake-shaped domain $\Omega \subset \mathbb{R}^2$. Recall that $\partial\Omega$ denotes the boundary of the lake, where we impose homogeneous Neumann conditions. Let $T > 0$ be the final time of interest. Further, suppose

$$B(\cdot, t), p(\cdot, t), P(\cdot, t) \in C([0, T], H^1(\Omega)) \cap L^2(0, T; H^2(\Omega)),$$

with

$$\frac{\partial B}{\partial n} = \frac{\partial p}{\partial n} = \frac{\partial P}{\partial n} = 0 \quad \text{on} \quad \partial\Omega \times (0, T),$$

where n is the outward normal. We define

$$V = \left\{ \phi \in H^1(\Omega) : \partial_n \phi|_{\partial\Omega} = 0 \right\}.$$

We will write v_1, v_2, v_3 for test functions associated with B, p, P , respectively. Given

$$\frac{\partial B}{\partial t} - \alpha \Delta B + \beta_B \vec{v}(t) \cdot \nabla B = r \left(1 - \frac{Q_m B}{p + \varepsilon} \right) h(B) B - l B - \frac{D}{z_m} B.$$

Multiply both sides by a test function $v_1 \in V$ and integrate over Ω :

$$\begin{aligned} \int_{\Omega} \frac{\partial B}{\partial t} v_1 dx - \alpha \int_{\Omega} \Delta B v_1 dx + \beta_B \int_{\Omega} (\vec{v} \cdot \nabla B) v_1 dx \\ = \int_{\Omega} \left[r \left(1 - \frac{Q_m B}{p + \varepsilon} \right) h(B) B - l B - \frac{D}{z_m} B \right] v_1 dx \end{aligned} \quad (22)$$

$$\begin{aligned} \implies \int_{\Omega} \frac{\partial B}{\partial t} v_1 dx + \alpha \int_{\Omega} \nabla B \cdot \nabla v_1 dx + \beta_B \int_{\Omega} (\vec{v} \cdot \nabla B) v_1 dx \\ = \int_{\Omega} \left[r \left(1 - \frac{Q_m B}{p + \varepsilon} \right) h(B) B - l B - \frac{D}{z_m} B \right] v_1 dx. \end{aligned} \quad (23)$$

We perform a similar method for p and P . Taking $v_2 \in V$ as the test function for the second equation, we see that

$$\begin{aligned} \int_{\Omega} \frac{\partial p}{\partial t} v_2 dx + \alpha \int_{\Omega} \nabla p \cdot \nabla v_2 dx + \beta_B \int_{\Omega} (\vec{v} \cdot \nabla p) v_2 dx \\ = \int_{\Omega} \left[\eta(B, p, P) - l p - \frac{D}{z_m} p \right] v_2 dx. \end{aligned}$$

and

$$\begin{aligned} \int_{\Omega} \frac{\partial P}{\partial t} v_3 dx + \beta \int_{\Omega} \nabla P \cdot \nabla v_3 dx + \beta_P \int_{\Omega} (\vec{v} \cdot \nabla P) v_3 dx \\ = \int_{\Omega} \left[\frac{D}{z_m} (P_h - P) - \eta(B, p, P) B + l p \right] v_3 dx. \end{aligned}$$

Let $\Delta t > 0$ be a uniform time step, and define times $t^n = n \Delta t$ for $n = 0, 1, \dots, N$ such that $N \Delta t = T$. A fully discrete backward Euler method for B is:

$$\begin{aligned} \int_{\Omega} \frac{B^{n+1} - B^n}{\Delta t} v_1 dx + \alpha \int_{\Omega} \nabla B^{n+1} \cdot \nabla v_1 dx + \beta_B \int_{\Omega} (\vec{v}^{n+1} \cdot \nabla B^{n+1}) v_1 dx \\ = \int_{\Omega} R_B(B^{n+1}, p^{n+1}) v_1 dx, \end{aligned}$$

where $R_B(\cdot)$ indicates the reaction terms

$$R_B(B^{n+1}, p^{n+1}) = r \left(1 - \frac{Q_m B^{n+1}}{p^{n+1} + \varepsilon} \right) h(B^{n+1}) B^{n+1} - l B^{n+1} - \frac{D}{z_m} B^{n+1}.$$

The forms for p and P are identical in structure, each having the discrete-time derivative, diffusion, advection, and reaction integrated against test functions. This set of discrete equations is then solved at each time step n using a nonlinear solver. The updated solutions $(B^{n+1}, p^{n+1}, P^{n+1})$ become the initial condition for the next step. After the final step N , we evaluate $Q^{n+1} = p^{n+1}/B^{n+1}$ in a pointwise manner. We

took the shoreline of the Pigeon Lake, Alberta, Canada provided by the provincial government in EPSG: 3400 system, and then we re-projected into EPSG: 4326, Fig. 15. We produced a two-dimensional triangular mesh using *gmsh*, an open-source 3D finite element mesh generator that provide a fast, lightweight for mesh generation (Geuzaine and Remacle 2009) ensuring element diameters around 50m on average. The boundary $\partial\Omega$ thus represents the lake perimeter, where we impose Neumann conditions. Real wind data $(u(t), v(t))$ were measured at hourly intervals. We aggregated these into a daily time series, then applied an Akima interpolation to obtain a smooth $\vec{v}(t)$ for each PDE time step. For each Δt in the solver, we update $\vec{v}(t)$ accordingly. This vector is assumed uniform in space. We use the Firedrake library (Ham 2023) to implement the aforementioned weak forms. We let V be a continuous Galerkin space of piecewise polynomials. We form the mixed function space $W = V \times V \times V \times V$, then defined

$$U = (B, p, P, Q) \in W, \quad v = (v_1, v_2, v_3, v_4) \in W.$$

We write the residual forms F_1, \dots, F_4 as in section 2, each integrated over Ω . The Neumann boundary condition is automatically enforced. We assemble these forms into a global problem $F(U) = 0$ in Firedrake,

$$F(U) = \sum_{i=1}^4 F_i(B, p, P, Q),$$

and solve with a backward Euler time discretization. Our code sets up a *Nonlinear-VariationalSolver* with an *ILU* or *bjacobi* preconditioner. After each time step, we update $U_n \leftarrow U$ and proceed until final time T_{final} . We also verified that artificially removing wind advection reproduced earlier purely diffusive solutions. After the 21-day simulation, we compared the modelled cyanobacterial biomass B (mgC/m^2) to the co-registered Sentinel-2 CE raster. Since CE is a unit-less reflectance ratio, both data sets were normalized to $[0, 1]$ before computing the scores:

$$\tilde{B}_i = \frac{B_i - \min_j B_j}{\max_j B_j - \min_j B_j + \varepsilon}, \quad \tilde{C}_i = \frac{C_i - \min_j C_j}{\max_j C_j - \min_j C_j + \varepsilon}, \quad (24)$$

where $i = 1, \dots, N$ enumerates the mesh nodes, C_i is the raw CE value mapped to the same node, and $\varepsilon = 10^{-12}$ avoids division by 0. The RMSE and the Pearson correlation (R) coefficient are then

$$\text{RMSE} = \sqrt{\frac{1}{N} \sum_{i=1}^N (\tilde{B}_i - \tilde{C}_i)^2}, \quad R = \frac{\sum_{i=1}^N (\tilde{B}_i - \bar{\tilde{B}})(\tilde{C}_i - \bar{\tilde{C}})}{\sqrt{\sum_{i=1}^N (\tilde{B}_i - \bar{\tilde{B}})^2} \sqrt{\sum_{i=1}^N (\tilde{C}_i - \bar{\tilde{C}})^2}}, \quad (25)$$

with \tilde{B} and \tilde{C} the spatial means of the normalized fields. For the 27 Aug 2023 validation scene, the process yields $\text{RMSE} = 0.121$ and $R = 0.857$.

Sobol indices

For the Sobol Indices, the first-order index for factor f at time t is defined as

$$S1_f(t) = \frac{\text{Var}[\mathbb{E}[B(t) | X_f]]}{\text{Var}[B(t)]},$$

while the total-order index is given by

$$ST_f(t) = 1 - \frac{\text{Var}[\mathbb{E}_{\sim f}[B(t) | f]]}{\text{Var}[B(t)]},$$

where $\mathbb{E}[B(t) | X_f]$ is the conditional expectation of $B(t)$ given X_f (the factor of interest), and $\mathbb{E}_{\sim f}[B(t) | f]$ denotes the expectation with respect to all parameters except f .

In our implementation, we generated 2048 samples for each analysis using Saltelli's extension of the Sobol sequence through the `SALib` Python library (Herman and Usher 2017). Each sampled configuration provides a unique set of parameter values. We considered the following ranges: $z_m \in [2.0, 10.0]$, $K_{bg} \in [0.1, 1.0]$, $D \in [0.01, 0.1]$, $P_h \in [0.0, 0.3]$, $\beta_B \in [0.01, 0.1]$. Each parameter set was used to initialize and solve our model for the entire time window, storing the resulting spatio-temporal evolution of $B(x, t)$. We then computed $S1_f(t)$ and $ST_f(t)$ across different time intervals and averaged over the spatial grid to assess how each parameter shapes the predicted cyanobacteria distribution. Additionally, to quantify how much variability in sensitivity arises spatially, we calculated the standard deviation of $(S1_f)_\ell$ and $(ST_f)_\ell$ over $\ell = 1, \dots, N_x N_y$, which provided the error bars in our final bar plots. Therefore, the mean impact of each parameter on cyanobacteria growth and the extent to which that impact varies across different spatial locations in the domain. For plotting purposes, we split the solution into smaller time bins of approximately 60 days to track how the relative influences of these parameters vary throughout the simulation.

Supplemental Figures

See Figs. 11, 12, 13, 14, 15, 16 and 17

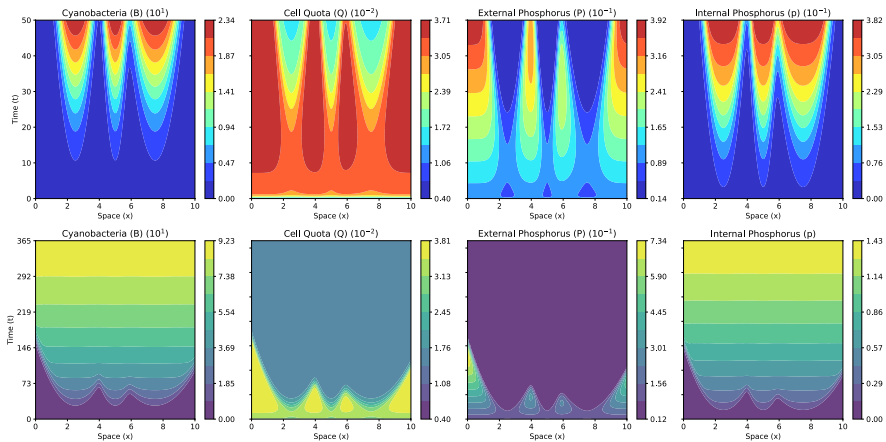


Fig. 11 Time series simulations in one dimension of cyanobacteria, cell quota, external and intracellular phosphorus over short (50 days) and long (365 days) time periods. There was no wind/movement incorporated for the solution

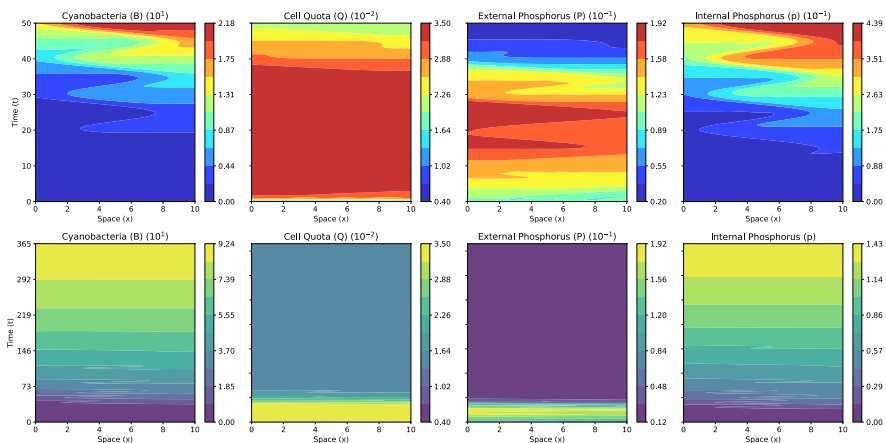


Fig. 12 Time series simulations in one dimension of cyanobacteria, cell quota, external and intracellular phosphorus over short (50 days) and long (365 days) time periods. We used an oscillatory wind function to simulate periodic movement

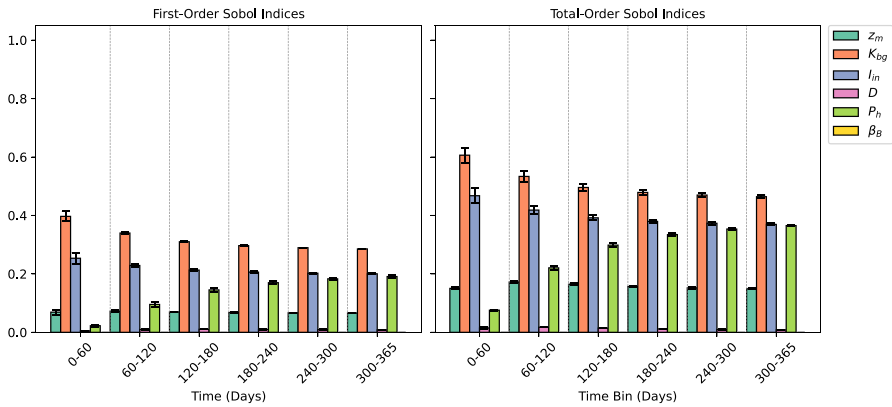


Fig. 13 Global sensitivity analysis using first- and total-order Sobol indices to compare the impact of physical lake conditions on the growth of cyanobacteria over space and time. The simulation is for 365 days, with contributions binned into 60 day intervals. There was no wind/movement incorporated for the solution

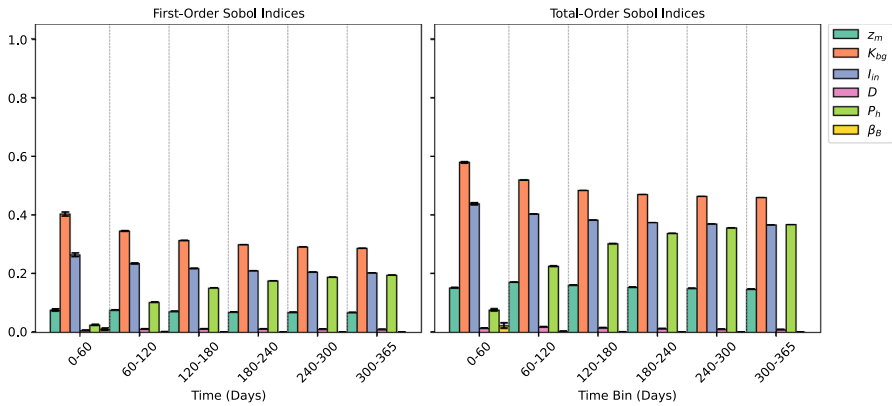


Fig. 14 Global sensitivity analysis using first- and total-order Sobol indices to compare the impact of physical lake conditions on the growth of cyanobacteria over space and time. The simulation is for 365 days, with contributions binned into 60 day intervals. We used an oscillatory wind function to simulate periodic movement

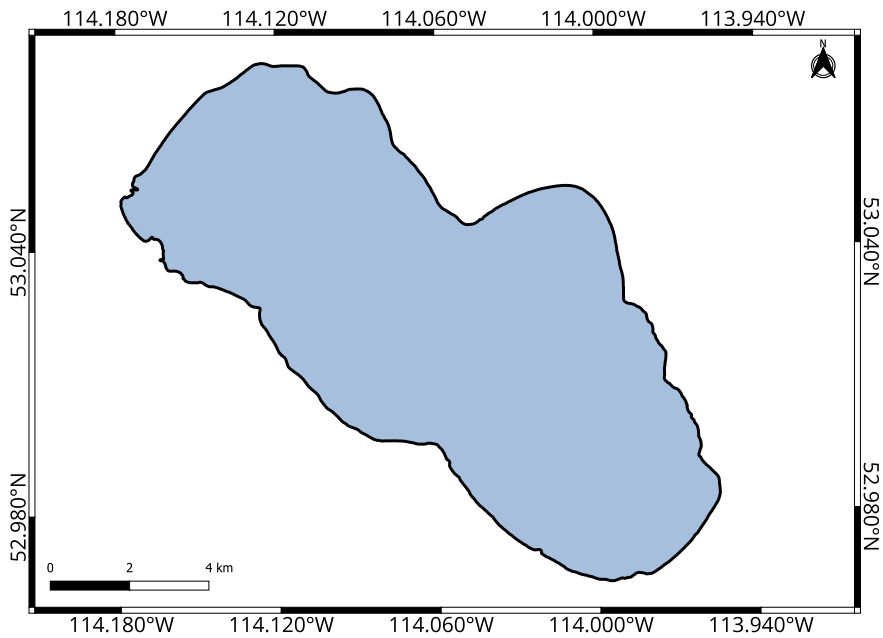


Fig. 15 Closed curve representing the shape of Pigeon Lake, Alberta, Canada. Provided by the Government of Alberta (2016)

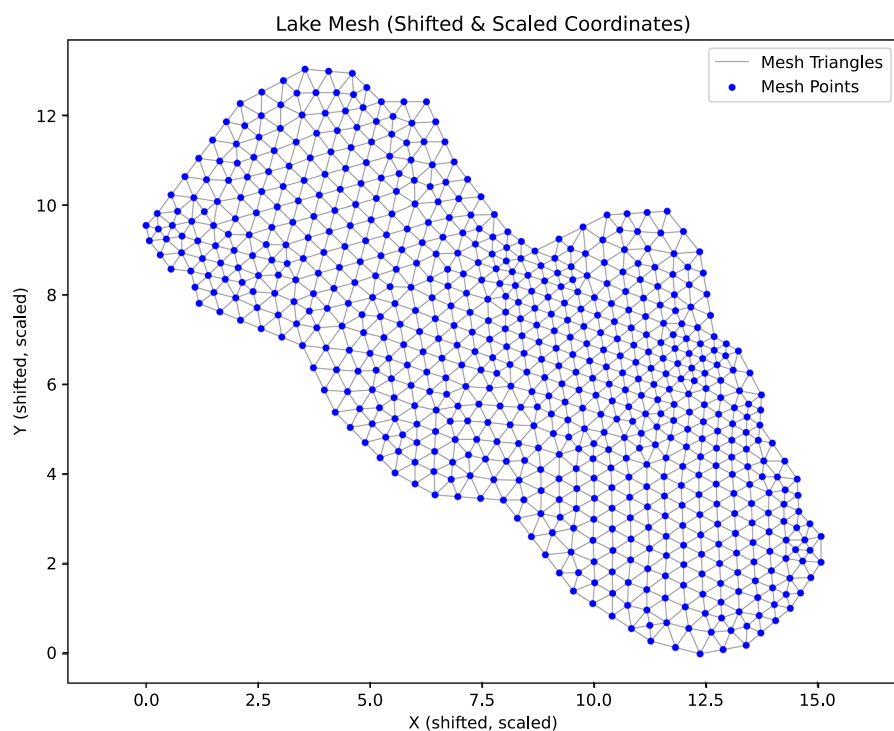


Fig. 16 Mesh of Pigeon Lake, Alberta, Canada that we solved our PDE system on

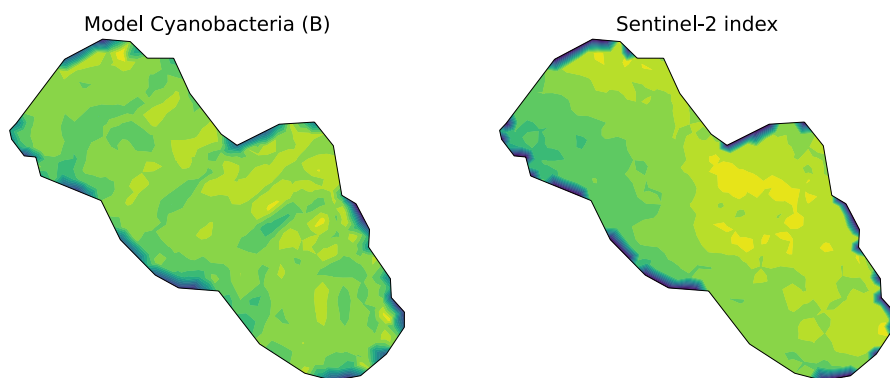


Fig. 17 Visual model comparison for validation after 21 days in Pigeon Lake, Alberta, Canada. Date shown is August 27, 2023. RMSE = 0.121, Pearson R Coefficient = 0.857

Acknowledgements This research project, especially J.S. and B.A.Z.L., was supported by a research grant (PI: H.W.) from Alberta Conservation Association. H.W.'s research was partially supported by an NSERC Individual Discovery Grant (RGPIN-2020-03911), an NSERC Discovery Accelerator Supplement Award (RGPAS-2020-00090), and a Senior Canada Research Chair.

Author contributions Jacob Serpico: Conceptualization, methodology, software, validation, formal analysis, data curation, writing, visualization, project administration. Kyunghan Choi: Methodology, software,

validation, formal analysis, writing. B.A. Zambrano-Luna: Conceptualization, methodology, software, data curation, writing, visualization. Tianxu Wang: Methodology, validation, formal analysis, writing. Hao Wang: Conceptualization, supervision, validation, writing, funding acquisition.

Code availability The code and data that support the findings of this study are available on GitHub with the identifier [Modelling cyanobacteria population and nutrient stoichiometry](#).

Declarations

Conflict of interest There are no conflict interests.

References


- Alberta Government (2016) Pigeon Lake, Alberta – Boundary (GIS data, polygon features). Alberta Energy Regulator. https://open.alberta.ca/dataset/gda-dig_2008_0828 Accessed 11 Feb 2025
- Amann H, Crandall MG (1990) Dynamic theory of quasilinear parabolic equations: II. Reaction-diffusion systems. *Differential Integral Equations* 3:13–75. <https://doi.org/10.57262/die/1371586185>
- Berger SA, Diehl S, Kunz TJ, Albrecht D, Oucible AM, Ritzer S (2006) Light supply, plankton biomass, and seston stoichiometry in a gradient of lake mixing depths. *Limnol Oceanogr* 51:1898–1905. <https://doi.org/10.4319/lo.2006.51.4.1898>
- Cantrell RS, Cosner C (2004) *Spatial Ecology via Reaction-Diffusion Equations*. John Wiley & Sons Ltd, Chichester
- Cao HS, Kong FX, Luo LC, Shi XL, Yang Z, Zhang XF, Tao Y (2006) Effects of wind and wind-induced waves on vertical phytoplankton distribution and surface blooms of *Microcystis aeruginosa* in Lake Taihu. *J Freshw Ecol* 21:231–238. <https://doi.org/10.1080/02705060.2006.9664991>
- Deng J, Chen F, Liu X, Peng J, Hu W (2016) Horizontal migration of algal patches associated with cyanobacterial blooms in an eutrophic shallow lake. *Ecol Eng* 87:185–193. <https://doi.org/10.1016/j.ecoleng.2015.12.017>
- Diehl S, Berger S, Woehrl R (2005) Flexible nutrient stoichiometry mediates environmental influences on phytoplankton and its resources. *Ecology* 86:2931–2945. <https://doi.org/10.1890/04-1512>
- Du C, Shi K, Liu N, Li Y, Lyu H, Yan C, Pan J (2022) Remote estimation of the particulate phosphorus concentrations in inland water bodies: a case study in Hongze Lake. *Remote Sens* 14(16):3863. <https://doi.org/10.3390/rs14163863>
- Evans LC (2010) *Partial Differential Equations*, 2nd edn. American Mathematical Society, Providence. <https://doi.org/10.1090/gsm/019>
- Gao L, Wang X, Johnson BA, Tian Q, Wang Y, Verrelst J, Mu X, Gu X (2020) Remote sensing algorithms for estimation of fractional vegetation cover using pure vegetation index values: a review. *ISPRS J Photogramm Remote Sens* 159:364–377. <https://doi.org/10.1016/j.isprsjprs.2019.11.018>
- Geuzaine C, Remacle JF (2009) Gmsh: a 3-D finite element mesh generator with built-in pre- and post-processing facilities. *Int J Numer Meth Eng* 79:1309–1331. <https://doi.org/10.1002/nme.2579>
- Ham DA, Kelly PHJ, Mitchell L, Cotter CJ, Kirby RC, Sagiyama K, Bouziani N, Vorderwuelbecke S, Gregory TJ, Betteridge J, Shapero DR, Nixon-Hill RW, Ward CJ, Farrell PE, Brubeck PD, Marsden I, Gibson TH, Homolya M, Sun T, McRae ATT, Luporini F, Lange M, Funke SW, Rathgeber F, Bercea GT, Markall GR (2023) *Firedrake User Manual*, 1st edn. Imperial College London and University of Oxford and collaborators. <https://doi.org/10.25561/104839>
- Heggerud CM, Wang H, Lewis MA (2020) Transient dynamics of a stoichiometric cyanobacteria model via multiple-scale analysis. *SIAM J Appl Math* 80:1223–1246. <https://doi.org/10.1137/19M1251217>
- Herman J, Usher W (2017) SALib: an open-source Python library for sensitivity analysis. [https://salib.github.io/SALib/Version 1.3.0](https://salib.github.io/SALib/Version%201.3.0)
- Hsu SB, Jiang J, Wang FB (2010) On a system of reaction–diffusion equations arising from competition with internal storage in an unstirred chemostat. *J Differ Equ* 248:2470–2496. <https://doi.org/10.1016/j.jde.2009.12.014>

- Hsu SB, Shi J, Wang FB (2014) Further studies of a reaction-diffusion system for an unstirred chemostat with internal storage. *Discrete Continuous Dyn Syst B* 19:3169–3189. <https://doi.org/10.3934/dcds.2014.19.3169>
- Hsu SB, Lam KY, Wang FB (2017) Single species growth consuming inorganic carbon with internal storage in a poorly mixed habitat. *J Math Biol* 75:1775–1825. <https://doi.org/10.1007/s00285-017-1134-5>
- Huisman J, Weissing FJ (1994) Light limited growth and competition for light in well mixed aquatic environments: an elementary model. *Ecology* 75:507–520. <https://doi.org/10.2307/1939554>
- Huisman J, Codd GA, Paerl HW et al (2018) Cyanobacterial blooms. *Nat Rev Microbiol* 16:471–483. <https://doi.org/10.1038/s41579-018-0040-1>
- Kalff J (2002) *Limnology: Inland Water Ecosystems*. Prentice Hall, Upper Saddle River
- Munoz Sabater J (2019) ERA5-Land monthly averaged data from 1981 to present. Copernicus Climate Change Service (C3S) Climate Data Store
- Okubo A, Levin S (2002) *Diffusion and Ecological Problems: Modern Perspectives*, 2nd edn. Springer, New York. <https://doi.org/10.1007/978-1-4757-4978-6>
- Paerl HW, Huisman J (2008) Blooms like it hot. *Science* 320:57–58. <https://doi.org/10.1126/science.1155398>
- Paerl HW, Huisman J (2009) Climate change: a catalyst for global expansion of harmful cyanobacterial blooms. *Environ Microbiol Rep* 1:27–37. <https://doi.org/10.1111/j.1758-2229.2008.00004.x>
- Paerl HW, Otten TG (2013) Harmful cyanobacterial blooms: causes, consequences, and controls. *Microb Ecol* 65:995–1010. <https://doi.org/10.1007/s00248-012-0159-y>
- Qin Q, Clark J, Voller V, Stefan H (2009) Depth-dependent dispersion coefficient for modeling of vertical solute exchange in a lake bed under surface waves. *J Hydraul Eng* 135:187. [https://doi.org/10.1061/\(ASCE\)0733-9429\(2009\)135:3\(187\)](https://doi.org/10.1061/(ASCE)0733-9429(2009)135:3(187))
- Reynolds CS (2006) *The Ecology of Phytoplankton*. Cambridge University Press, Cambridge
- Sobol IM (2001) Global sensitivity indices for nonlinear mathematical models and their Monte Carlo estimates. *Math Comput Simul* 55:271–280. [https://doi.org/10.1016/S0378-4754\(00\)00270-6](https://doi.org/10.1016/S0378-4754(00)00270-6)
- Wang H, Smith HL, Kuang Y, Elser JJ (2007) Dynamics of stoichiometric bacteria–algae interactions in the epilimnion. *SIAM J Appl Math* 68:503–522. <https://doi.org/10.1137/060665919>
- Wang H, Venegas Garcia P, Ahmed S, Heggerud CM (2022) Mathematical comparison and empirical review of the Monod and Droop forms for resource-based population dynamics. *Ecol Model* 466:109887. <https://doi.org/10.1016/j.ecolmodel.2022.109887>
- Wang TX, Sim J, Wang H (2025) Existence and asymptotic stability of a generic Lotka-Volterra system with nonlinear spatially heterogeneous cross-diffusion. *J Differential Equ* 434:113302
- Wilhelm SW, Farnsley SE, LeClerc GR, Layton AC, Satchwell MF, DeBruyn JM, Boyer GL, Zhu G, Paerl HW (2011) The relationships between nutrients, cyanobacterial toxins and the microbial community in Taihu (Lake Tai). *China Harmful Algae* 10(2):207–215. <https://doi.org/10.1016/j.hal.2010.10.001>
- Zambrano-Luna BA, Milne R, Wang H (2025) Cyanobacteria hot spot detection integrating remote sensing data with convolutional and Kolmogorov-Arnold networks. *Sci Total Environ* 960:178271. <https://doi.org/10.1016/j.scitotenv.2024.178271>
- Zhang Y, Loisel S, Shi K, Han T, Zhang M, Hu M, Jing Y, Lai L, Zhan P (2021) Wind effects for floating algae dynamics in eutrophic lakes. *Remote Sens* 13(4):800. <https://doi.org/10.3390/rs13040800>
- Zhang Y, Jin S, Wang N, Zhao J, Guo H, Pellikka P (2022) Total phosphorus and nitrogen dynamics and influencing factors in Dongting Lake using Landsat data. *Remote Sensing* 14(22):5648. <https://doi.org/10.3390/rs14225648>
- Zhao L, Huang W (2014) Models for identifying significant environmental factors associated with cyanobacterial bloom occurrence and for predicting cyanobacterial blooms. *J Great Lakes Res* 40(2):265–273. <https://doi.org/10.1016/j.jglr.2014.02.011>

Publisher's Note Springer Nature remains neutral with regard to jurisdictional claims in published maps and institutional affiliations.

Springer Nature or its licensor (e.g. a society or other partner) holds exclusive rights to this article under a publishing agreement with the author(s) or other rightsholder(s); author self-archiving of the accepted manuscript version of this article is solely governed by the terms of such publishing agreement and applicable law.

Authors and Affiliations

Jacob Serpico¹ · Kyung-Han Choi¹ · B. A. Zambrano-Luna¹ · Tian Xu Wang¹ · Hao Wang¹ 

✉ Hao Wang
hao8@ualberta.ca

¹ Interdisciplinary Lab for Mathematical Ecology and Epidemiology & Department of Mathematical and Statistical Sciences, University of Alberta, Edmonton, AB T6G 2R3, Canada